Draft version July 27, 2016
Preprint typeset using LaTeX style emulateapj v. 01/23/15

arXiv:1604.01764v2 [astro-ph.GA] 26 Jul 2016

THE MASSIVE SURVEY IV.: THE X-RAY HALOS OF THE MOST MASSIVE EARLY-TYPE GALAXIES IN THE NEARBY UNIVERSE

Andy D. Goulding[1], Jenny E. Greene[1], Chung-Pei Ma[2], Melanie Veale[2], Akos Bogdan[3], Kristina Nyland[4], John P. Blakeslee[5], Nicholas J. McConnell[5] & Jens Thomas[6]

[1]Department of Astrophysical Sciences, Princeton University, Princeton, NJ
[2]Department of Astronomy, University of California, Berkeley, CA
[3]Harvard-Smithsonian Center for Astrophysics, Cambridge, MA
[4]National Radio Astronomy Observatory, 520 Edgemont Road, Charlottesville, VA
[5]Herzberg Astronomy and Astrophysics, Victoria, BC, Canada and
[6]Max-Planck Institute for Extraterrestrial Physics, Giessenbachstr. 1, Garching, Germany

Draft version July 27, 2016

ABSTRACT

Studies of the physical properties of local elliptical galaxies are shedding new light on galaxy formation. Here we present the hot gas properties of 33 early-type systems within the MASSIVE galaxy survey that have archival *Chandra* X-ray observations, and use these data to derive X-ray luminosities ($L_{\rm X,gas}$) and plasma temperatures ($T_{\rm gas}$) for the diffuse gas components. We combine this with the ATLAS$^{\rm 3D}$ survey to investigate the X-ray–optical properties of a statistically significant sample of early-type galaxies across a wide range of environments. When X-ray measurements are performed consistently in apertures set by the galaxy stellar content, we deduce that all early-types (independent of galaxy mass, environment and rotational support) follow a universal scaling law such that $L_{\rm X,gas} \propto T_{\rm gas}^{\sim 4.5}$. We further demonstrate that the scatter in $L_{\rm X,gas}$ around both K-band luminosity (L_K) and the galaxy stellar velocity dispersion (σ_e) is primarily driven by $T_{\rm gas}$, with no clear trends with halo mass, radio power, or angular momentum of the stars. It is not trivial to tie the gas origin directly to either stellar mass or galaxy potential. Indeed, our data require a steeper relation between $L_{\rm X,gas}$, L_K, and σ_e than predicted by standard mass-loss models. Finally, we find $T_{\rm gas}$ is set by the galaxy potential inside the optical effective radius. We conclude that within the inner-most 10–30 kpc region, early-types maintain pressure-supported hot gas, with a minimum $T_{\rm gas}$ set by the virial temperature, but the majority show evidence for additional heating.

Subject headings: galaxies: normal – X-rays: galaxies

1. INTRODUCTION

Despite decades of active research, the assembly history and evolution of the most massive elliptical galaxies in the Universe remains a widely unanswered question. The current consensus is that the most massive early-type galaxies formed the majority of their stars at high-redshift ($z > 2$; Blakeslee et al. 2003; Thomas et al. 2005; van Dokkum et al. 2010), and have since grown via mergers (e.g., Bell et al. 2004; Faber et al. 2007; Cowie & Barger 2008; Bundy et al. 2010). These mergers, coupled with more minor accretion events of satellite systems, imparts substantial quantities of gaseous material into the parent galaxy halo (e.g., van Dokkum et al. 2008). Elliptical galaxies are known to possess relatively low star-formation rates, typically orders of magnitude below those found in their spiral counterparts. Hence, it is unclear which mechanisms prevent the gas from cooling, and forming new stars, in early-type galaxies.

Massive elliptical galaxies are surrounded by a hot interstellar medium (ISM) that may have initially formed due to shock heating of the cooling gas during its entrapment within the galaxy's deep potential (Forman et al. 1985; Trinchieri & Fabbiano 1985) and/or from stellar mass that was lost from evolved stars (e.g., Mathews 1990; Brighenti & Mathews 1997; Mathews & Brighenti 2003). These gas halos are often extended well beyond the stellar distribution of the galaxy, and can be used to probe the dark halo mass by assuming that the gas is in virial equilibrium out to large radii (Canizares et al. 1987).

Two of the most fundamental measurables of the X-ray emitting thermal ISM are its luminosity ($L_{\rm X,gas}$) and gas temperature ($T_{\rm gas}$). These observables reflect the physics related to the baryons within the system, and are directly linked to the total entropy and gas mass. With the advent of the Einstein and ROSAT X-ray telescopes, it became possible to study the hot ISM of statistically significant samples of ellipticals. Thus, it is now well established that $L_{\rm X,gas}$ and $T_{\rm gas}$ are strongly correlated in massive virialized clusters, going as $L_{\rm X,gas} \propto T_{\rm gas}^{2-3}$ (e.g., Mitchell et al. 1979; Mushotzky 1984; Edge & Stewart 1991; Markevitch 1998; Ettori et al. 2004; Mittal et al. 2011; Maughan et al. 2012). On group/poor-cluster scales, the relation steepens ($L_{\rm X,gas} \propto T_{\rm gas}^{3-4}$; Wu et al. 1999; Helsdon & Ponman 2000; Mulchaey 2000; Osmond & Ponman 2004) as baryon physics (e.g., feedback from active galactic nuclei; galaxy-scale winds; cooling flows) begins to dominate over gravity, causing deviations from the self-similar scaling relation ($L_{\rm X,gas} \propto T_{\rm gas}^{2}$) expected in fully gravitationally collapsed systems. The $L_{\rm X,gas}$–$T_{\rm gas}$ relation may further steepen in the poorest-groups and individual galaxy halos as the hot gas surrounding the galaxies is no longer virialized and/or is dominated by other effects. Previous studies have sought to link these

Email:- goulding@astro.princeton.edu

differing structural scales to provide a coherent picture of the X-ray properties of the most massive systems in the Universe (e.g., O'Sullivan et al. 2003; Khosroshahi et al. 2007; Sun et al. 2007; Diehl & Statler 2008; Sun et al. 2009; Mulchaey & Jeltema 2010; Vajgel et al. 2014). However, observational evidence for the hot gas origin is still in question. It has yet to be well established to what extent the gas properties are influenced by the effects of cooling versus external agents (such as accretion, stripping, sloshing, shocks), and at a given stellar mass, the dependence of the gas luminosity and/or temperature on environment (e.g., White & Sarazin 1991; Brown & Bregman 2000; O'Sullivan et al. 2001; Helsdon et al. 2001).

Given their substantially lower $L_{\rm X,gas}$, the hot gas properties of individual elliptical galaxies are less well known. However, successive generations of X-ray telescopes, with improved sensitivity, larger effective areas, and superior spatial resolution are now beginning to allow a more in-depth study of the hot gas component in unprecedented detail, which in turn sheds new light on the formation history of galaxies. Using the excellent angular resolution of the *Chandra* X-ray telescope, studies are directly detecting and isolating the X-ray emission from stellar processes such as the low mass X-ray binary population that have plagued the previous generation of X-ray telescopes, particularly in the low stellar-mass regime (e.g., Sivakoff et al. 2004; Boroson et al. 2011; Lehmer et al. 2014), as well as exploring the X-ray halos in early-type galaxies as a function of cosmic time (e.g., Lehmer et al. 2007; Civano et al. 2014; Paggi et al. 2015), and probing the thermal gas content (e.g., Diehl & Statler 2007; Jeltema et al. 2008; Memola et al. 2009; Bogdán et al. 2012a,b; Kim & Fabbiano 2013; Su et al. 2015; Kim & Fabbiano 2015).

On a galaxy-wide scale, insight into the sources and retention of the hot gas may be gained by correlating the X-ray properties and optical properties of the galaxies. Given the expected origins (e.g., stellar mass loss; stellar feedback) of the hot gas, to zeroth order, one might imagine that $L_{\rm X,gas}$ would correlate with the stellar mass (M_*) of the galaxy. However, the observed scatter in the $L_{\rm X,gas} - M_*$ relation is larger than this simple expectation, requiring subsequent studies to assess if additional physical parameters can explain the scatter in the relation. Obvious physical properties that may drive the scatter include the large-scale environment, the presence of an AGN, and the rotation properties of the host galaxy.

In general, early-type galaxies are thought to fall into two families (e.g., Bender et al. 1989; Kormendy & Bender 1996, 2012). Typically lower-mass galaxies tend to have net rotation (fast rotators; Emsellem et al. 2007), disky isophotes, and a power-law light distribution that continues all the way to their centers (e.g., Faber et al. 1997; Lauer et al. 2007). By contrast, the most massive elliptical galaxies tend to be completely dispersion dominated (slow rotators), have boxy isophotes, and have a light deficit in their center known as a core (e.g., Ferrarese et al. 1994; Lauer et al. 1995; Ferrarese et al. 2006; Kormendy et al. 2009). Generally, it is thought that the fast rotators have dissipation in their most recent merger history, while slow rotators have suffered a number of dry mergers, and binary black hole scouring has left a core in their center (e.g., Krajnović et al. 2013 and references there-in). Integral field unit (IFU) observations provide high-fidelity measurements of the rotation/angular-momentum of early-type galaxies (Emsellem et al. 2011).

Earlier work has focused on the ATLAS$^{\rm 3D}$ sample (e.g., Emsellem et al. 2011; Cappellari et al. 2013; Krajnović et al. 2011; Young et al. 2011), a volume-limited sample ($D < 42$ Mpc) of all nearby early-type galaxies with $M_K < -21.5$ mags. Using the ATLAS$^{\rm 3D}$ galaxies, there has been suggestive evidence that galaxies with net rotation (i.e., fast rotators) have lower L_X than slow rotators at a given stellar mass. However, due in part to the limited volume, the ATLAS$^{\rm 3D}$ sample contains few slow rotating systems with available high-resolution X-ray data, and virtually no galaxies with stellar masses above $M_* > 10^{11}\,{\rm M}_\odot$. Complementary to these previous multi-wavelength studies, here we focus our study on the hot gas emission present in the volume-limited MASSIVE survey (Ma et al. 2014; M14 hereafter) of the 116 most massive early-type galaxies within 108 Mpc. Similar to ATLAS$^{\rm 3D}$, MASSIVE uses integral-field spectroscopy (IFS) combined with uniform K-band imaging to study the stellar populations (Greene et al. 2015) and stellar kinematics (Veale et al., in prep.) of the MASSIVE galaxies.

In this paper, we investigate the connection between the X-ray and optical properties of massive early-type galaxies in the nearby Universe by combining the volume-limited MASSIVE sample with the nearby sample of ellipticals in the ATLAS$^{\rm 3D}$ survey. In section 2 we present the MASSIVE sample, the optical spectral measurements from our integral field unit spectroscopy, and the comparison sample derived from the ATLAS$^{\rm 3D}$ survey. In section 3, we provide the data reduction and spectral fitting analyses of the *Chandra* X-ray data for the 33 MASSIVE galaxies with appropriate X-ray data. In section 4, we discuss the X-ray and optical properties of the combined MASSIVE and ATLAS$^{\rm 3D}$ samples, and show evidence that when the X-ray luminosity and gas temperatures are measured within physically-motivated apertures, set by the galaxy stellar content, these measurables correlate significantly, and are driven primarily by the small-scale galaxy potential. Finally, in section 5 we summarize our findings. Throughout the manuscript we adopt a flat ΛCDM cosmology with $H_0 = 71\,{\rm km\,s^{-1}\,Mpc^{-1}}$ and $\Omega_M = 0.3$.

2. THE MASSIVE GALAXY SAMPLE AND AUXILIARY DATA

2.1. *The MASSIVE Survey*

MASSIVE is a volume-limited sample of the 116 most massive early-type galaxies within 108 Mpc. The selection and sample properties are described in detail in Ma et al. (2014); we summarize salient details here for completeness. To emulate a stellar mass selection, we select galaxies from the 2MASS Redshift Survey (2MRS; Huchra et al. 2012) that are brighter than a total $K-$band magnitude limit of $M_K < -25.3$ mag ($\approx 10^{11.5}\ M_\odot$). We additionally apply a morphological cut based on the Hyperleda database (Paturel et al. 2003) to remove large spiral and interacting galaxies. The large-scale environment, group numbers and halo masses are taken from the 2MASS-based high-density

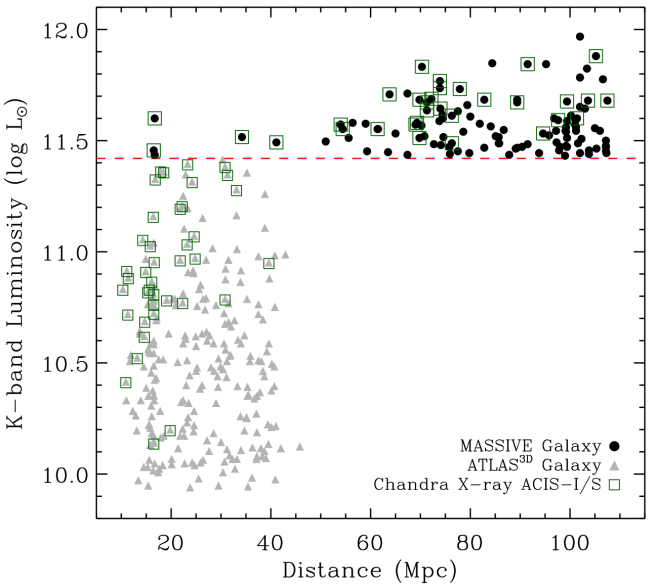

FIG. 1.— Logarithm of 2MASS total K-band luminosity in units of solar luminosities versus distance for the MASSIVE galaxy sample (filled circles). The red dashed line represents the total K-band cut of $M_K < 25.3$ magnitudes, which was used to define the initial MASSIVE sample selection presented in Ma et al. (2014). As a comparison, the ATLAS^{3D} galaxy sample is shown with gray triangles. The sub-sample of galaxies with publicly available archival *Chandra* X-ray ACIS-I or ACIS-S observations are additionally highlighted with open green squares.

contrast (HDC) group catalog of Crook et al. (2007). The HDC catalog is constructed using a Friends-of-Friends algorithm; it contains lists of galaxy membership in groups that have a density contrast of ≥ 80, and is complete to $\sim L^*$ galaxy mass at ≈ 70 Mpc. The resulting 116 early-type galaxies span a range of stellar velocity dispersion ($\sim 180 - 400$ km/s) and are found in a wide array of environments, from "field" galaxies with no $\sim L^*$ companions to rich clusters (Coma, Perseus, and Virgo).

The core science goals of the MASSIVE survey are driven by the need for wide-format integral field unit spectroscopy taken with the Mitchell Spectrograph (Hill et al. 2008) on the 2.7m Harlan J. Smith telescope at the McDonald Observatory. The large field of view of the Mitchell Spectrograph ($107\times107''$) is well-suited to the study of massive nearby galaxies. To date, we have IFU spectroscopy for 70 of the 116 galaxies in the MASSIVE survey. With these data we are measuring stellar population gradients (Greene et al. 2013, 2015), molecular gas masses and star-formation efficiencies (Davis et al. 2016), stellar kinematic fields (Veale et al. in prep), and when combined with modeling, the enclosed dark matter halo mass (e.g. Thomas et al. 2011).

2.2. *Effective Radii Measurements*

We adopt single Sérsic (1963) fits to the light profiles to derive the half-light radii. For roughly two thirds of our sample, we have Sloan Digital Sky Survey (SDSS; York et al. 2000) imaging. For these galaxies, we use the NASA-Sloan Atlas (Blanton & Moustakas 2009) catalog effective-radius (R_e) measurements. For the remaining galaxies that do not have SDSS imaging, we adapt a size measurement from 2MASS (Jarrett et al. 2003). We fit a linear conversion relation to correct the 2MASS measurements to match the SDSS measurements, such that $\log_{10}(\mathrm{R_{e,2MASS}}) = 0.8\log_{10}(\mathrm{R_{e,SDSS}}) - 0.076$ (Ma et al. 2014, their Eq. 4), where $R_{\mathrm{e,2MASS}}$ is the median effective radius measured from the JHK band 2MASS imaging.[1]

2.3. *Spectral Measurements*

The galaxy kinematics are derived from the optical IFU spectra. Full details of our kinematic measurements will be described in Veale et al. in preparation, but for completeness we summarize the data and analysis methodology here. Veale et al. bin the fibers in the galaxies to ensure a S/N> 20 per spatial bin. In conjunction with the MILES (Sánchez-Blázquez et al. 2006; Falcón-Barroso et al. 2011) stellar template library, they use the penalized pixel-fitting (pPXF) method (Cappellari & Emsellem 2004) to measure the line-of-sight velocity distribution, which is parameterized using Gauss-Hermite expansions. Six Gauss-Hermite moments are fit for each spectrum to measure the velocity (V), velocity dispersion (σ_*), and the subsequent higher-order kinematical moments h_3, h_4, h_5, h_6.

In this work, we will use the luminosity-weighted σ_* measurements within R_e from Veale et al. We are also interested in the angular momentum content of the galaxies. As in the ATLAS^{3D} project, we use a two-dimensional version of V/σ, $\lambda_R \sim \langle R|V|\rangle/\langle R\sqrt{V^2+\sigma_*^2}$ (Binney 2005; Emsellem et al. 2007), to quantify the angular momentum content of the galaxies as a function of radius. Emsellem (2013) define the threshold between slow and fast rotators, as $\lambda_R(\mathrm{slow}) < 0.3\sqrt{\epsilon}$, and we adopt their definition here for ease of comparison with the ATLAS^{3D} (see Table 1). At least eighteen out of the 33 MASSIVE galaxies studied here are unequivocally slow rotators.

2.4. *The Archival Chandra X-ray Sample*

The Advanced CCD Imaging Spectrometer (ACIS) on-board the *Chandra* X-ray Observatory provides an exquisite view of the X-ray universe to an unprecedented angular resolution ($\sim 0.49''$/pixel). For example, the 75% encircled energy fraction (EEF) of XMM-*Newton* is $\sim 20''$, which corresponds to ~ 7 kpc at 70 Mpc. By contrast, *Chandra* has a 90% EEF within $1''$ at $E \sim 0.5$–2 keV. Thus, *Chandra* has been used to great effect to accurately measure the X-ray properties of local early-type systems, and directly remove contaminants (e.g., from stellar sources) from measurements of the diffuse gas halo. To ensure a more homogeneous dataset, and to provide the most accurate measurements of the hot ISM, here we choose to harness the *Chandra* observatory to provide the X-ray imaging and spectroscopy for the MASSIVE galaxies.

To date, 39 of the 116 galaxies in the MASSIVE sample have publicly available *Chandra* ACIS-I and/or ACIS-S observations. These observations were performed as part of a multitude of different scientific programs. These sources cover a wide range of total exposure times ($\sim$ 2–300 ks), with some observations occurring more than a decade apart. While heterogeneous in construction, this X-ray sample still provides a representative subset ($\approx$

[1] We note that it is well established that the 2MASS size measurement typically underestimates the galaxy size relative to the SDSS measurement (Lauer et al. 2007; Kormendy et al. 2009)

TABLE 1
The MASSIVE X-ray sample

Common Name	α_{J2000}	δ_{J2000}	z	D_L	L_K	$N_{H,gal}$	σ_e	R_e	ϵ	λ_{R_e}	X-ray AGN?	# of Neighbor	Cent. Gal?	$M_{\rm Halo}$	$P_{1.4\rm GHz}$
	(degrees)			(Mpc)	($L_\odot$)	$\times10^{20}$	(km/s)	($''$)						(log $M_\odot$)	(log W/Hz)
(1)	(2)		(3)	(4)	(5)	(6)	(7)	(8)	(9)	(10)	(11)	(12)	(13)	(14)	(15)
NGC0057	3.8787	17.3284	0.0181	76.3	11.61	3.86	253	27.0	0.17	0.02	-	1	-	<11.0	20.30
NGC0315	14.4538	30.3524	0.0165	70.3	11.83	5.83	341	25.1	0.28	0.06	✓	6	✓	13.4	23.66
NGC0383	16.8540	32.4126	0.0170	71.3	11.63	5.40	257	20.5	0.14	0.25	✓	29	-	14.3	23.82
NGC0410	17.7453	33.1520	0.0177	71.3	11.67	5.34	246	31.6	0.25	0.04	-	29	✓	14.3	21.54
NGC0499	20.7978	33.4601	0.0147	69.8	11.51	5.33	266	15.6	-	-	-	35	-	14.5	20.22
NGC0507	20.9164	33.2561	0.0165	69.8	11.68	5.25	257	38.4	0.09	0.05	✓	35	✓	14.5	20.22
NGC0533	21.3808	1.7590	0.0185	77.9	11.73	3.00	259	40.7	0.26	0.04	-	3	✓	13.8	22.31
NGC0547	21.5024	-1.3451	0.0178	74.0	11.64	4.03	232	19.7	0.14	0.07	-	32	-	14.3	22.59†
NGC0708	28.1937	36.1518	0.0162	69.0	11.57	5.30	209	65.1	0.40	0.05	-	39	✓	14.5	22.57
NGC0741	29.0874	5.6289	0.0185	73.9	11.74	4.50	291	26.9	0.17	-	-	5	✓	13.7	21.91†
NGC0777	30.0622	31.4294	0.0167	72.2	11.69	4.80	292	18.6	0.17	0.05	-	7	✓	13.4	21.64
NGC1129	43.6141	41.5796	0.0173	73.9	11.77	9.91	261	30.2	0.04	0.07	-	33	✓	14.7	20.27
NGC1132	43.2159	-1.2747	0.0231	97.6	11.59	5.46	215	30.9	0.37	0.05	-	3	✓	13.6	21.78
NGC1600	67.9161	-5.0861	0.0156	63.8	11.71	4.80	303	55.3	0.26	0.02	-	16	✓	14.2	22.47
NGC1700	74.2347	-4.8658	0.0130	54.4	11.55	4.00	231	31.9	0.28	0.14	-	4	✓	12.6	20.00
NGC2340	107.7950	50.1747	0.0198	89.4	11.67	7.41	231	51.7	0.44	0.03	-	18	-	14.1	20.92†
NGC2783	138.4145	29.9929	0.0225	101.4	11.60	2.10	268	38.2	0.39	0.05	-	3	✓	12.3	22.47
NGC2832	139.9453	33.7498	0.0232	105.2	11.88	1.59	295	21.2	0.31	0.05	-	4	✓	13.8	20.58
NGC3209	155.1601	25.5050	0.0209	94.6	11.53	1.95	303	29.4	-	-	-	3	✓	11.9	21.07†
NGC3842	176.0090	19.9498	0.0211	99.4	11.67	2.00	230	24.2	0.22	0.03	-	42	✓	14.7	22.15
NGC4073	181.1128	1.8960	0.0196	91.5	11.84	1.80	289	23.0	0.32	0.02	-	10	✓	14.0	20.46
NGC4472	187.4450	8.0004	0.0033	16.7	11.60	1.66	289	181.8	0.17	0.08	-	205	✓	15.0	21.86
NGC4555	188.9216	26.523	0.0223	103.6	11.68	1.36	268	29.8	0.20	0.13	-	1	-	<11.0	21.40†
NGC4649	190.9167	11.5526	0.0037	16.5	11.46	2.20	340	44.1	0.16	0.13	-	205	-	15.0	20.98
NGC5129	201.0417	13.9765	0.0230	107.5	11.68	1.70	222	21.8	0.37	0.41	-	1	-	<11.0	21.99
NGC5322	207.3133	60.1904	0.0059	34.2	11.52	1.64	239	20.1	0.33	0.07	✓	8	✓	13.5	22.04
NGC5353	208.3613	40.2831	0.0078	41.1	11.49	0.98	290	27.8	-	-	-	12	✓	13.3	21.91
NGC6482	267.9534	23.0719	0.0131	61.4	11.55	7.74	301	22.4	0.36	0.10	-	3	✓	13.0	20.11
NGC7052	319.6377	26.4469	0.0156	69.3	11.58	13.60	284	35.8	0.50	-	✓	1	-	<11.0	22.96
NGC7265	335.6145	36.2098	0.0170	82.8	11.68	12.90	214	39.8	0.22	0.05	-	21	✓	14.6	20.37
NGC7618	349.9468	42.8526	0.0173	76.3	11.49	11.90	298	21.6	-	-	✓	10	✓	13.6	22.42
NGC7619	350.0605	8.2063	0.0125	54.0	11.57	5.00	273	34.6	0.23	0.13	-	12	✓	13.9	21.84
NGC7626	350.1772	8.2170	0.0114	54.0	11.57	5.03	251	26.7	0.14	0.03	✓	12	-	13.9	22.96

Notes:- [1]Common galaxy name; [2]J2000 positional co-ordinates from the NASA Extra-galactic Database (NED); [3]Spectroscopic redshift; [4]Luminosity distance in Megaparsecs assuming $H_0 = 71\,{\rm km\,s^{-1}\,Mpc^{-1}}$ and $\Omega_\Lambda = 0.70$ and corrected for non-cosmological flows; [5]Extinction-corrected total absolute K-band luminosity; [6]Galactic Neutral hydrogen column density in units of $10^{20}\,{\rm cm^{-2}}$; [7]Stellar velocity dispersion in units of km/s (Veale et al. in prep.); [8]Effective radius from optical and near-IR imaging in units of arc-seconds; [9]Ellipticity, such that $\epsilon = 1 - b/a$; [10]2-D galaxy rotation parameter, such that $\lambda_R \sim \langle R|V|\rangle/\langle R\sqrt{V^2+\sigma_*^2}$ measured in our IFU data (Veale et al. in prep.). Those sources marked with '-' currently lack sufficient IFU data for an accurate determination of their rotation parameter; [11]Evidence for an X-ray point source in the nuclear region in the 4–7 keV band; [12]Number of neighbors present in the galaxy group/cluster; [13]Is the source considered to be at the center of the group/cluster?; [14]Logarithmic total mass of the large environment halo in solar masses (Crook et al. 2007); [15]Logarithmic radio power at 1.4 GHz in units of W/Hz from the NVSS or FIRST (†) catalog.

1/4) of the whole MASSIVE survey. Of the 39 MASSIVE galaxies with available data, we determine that the *Chandra* observations for three galaxies (NGC 3862, NGC 5252, M87) are heavily contaminated by a central point-source that dominates the X-ray emission, and are thus subject to significant pile-up effects. Hence, we choose to remove these three sources from the sample, given the significant measurement uncertainties introduced due to modeling of the pile-up effects and separation of the AGN and diffuse emission.[2] We also do not include satellites within the Coma cluster due to the difficulties in separating the galaxy ISM from the intra-cluster medium at $\sim$ 100 Mpc (e.g., NGC 4874; NGC 4889) or the galaxy ISM being subject to ram-pressure stripping (e.g., NGC 4839). Our final X-ray sample consists of 33 galaxies (see Figure 1).

[2] We note that two further galaxies (NGC 315; NGC 383) have prominent X-ray emission produced by central AGN. These observations are not subject to significant pile-up and do not contribute significantly to the total X-ray emission. Hence, we accurately include the AGN contribution to the diffuse ISM component in our spectral fitting analysis. Thus, our MASSIVE X-ray galaxy sample does not include an explicit bias against systems that are actively growing their central supermassive black holes.

2.5. *ATLAS^{3D}: A representative lower mass comparison sample of nearby early-type galaxies*

To place the MASSIVE galaxy sample into the wider context of galaxy evolution, we require a comparison sample of lower mass early-type systems that have similar quality optical and X-ray data. In order to mitigate systematic effects that can dominate samples that have been gathered from multiple datasets and/or investigations, this comparison sample should be derived from a single homogeneous survey. The ATLAS^{3D} project is a volume-limited sample of all nearby early-type galaxies within 42 Mpc selected from the 2MRS with $M_K < -21.5$ mags (see Cappellari et al. 2011). The ATLAS^{3D} sources have optical IFU spectroscopy using the SAURON instrument (Bacon et al. 2001) on the William Herschel Telescope. The near-infrared selection of systematically lower mass systems combined with their optical ancillary data makes the ATLAS^{3D} project the ideal comparison

sample for MASSIVE. Most recently, Kim & Fabbiano (2015) presented constrained X-ray temperature and luminosity measurements for 49 (of 61) early-type galaxies in ATLAS^{3D} that have observations with the *Chandra* X-ray telescope. These X-ray measurements were performed using large extraction apertures irrespective of the angular size of the galaxy observed in the optical or near-IR. Complementary to the study of Kim & Fabbiano (2015), Su et al. (2015) present X-ray measurements for a sub-sample of the Kim & Fabbiano (2015) objects with X-ray measurements performed within apertures defined by the effective radius of the galaxy (see Section 3 of this work). As a comparison sample to our MASSIVE survey, we include measurements from both of these studies, as well as additional X-ray measurements for other ATLAS^{3D} galaxies, and updated measurements for a further subset of the objects presented in Su et al. (2015) (see Appendix). After removal of objects that have X-ray measurements adversely affected by AGN emission and source overlap between MASSIVE and ATLAS^{3D}, our comparison ATLAS^{3D} galaxy sample contains 41 sources.

3. CHANDRA X-RAY ANALYSIS

In this section we describe the data reduction, imaging analysis, and spectral analysis of the 33 MASSIVE galaxies with publicly available archival *Chandra* X-ray observations. Of the 33 galaxies, 32 have observations performed in the ACIS-S mode, while NGC 1129 was performed in ACIS-I. The individual observation identification numbers (ObsIDs), and the basic observation information are provided in Table 2.

3.1. *Data reduction and point source removal*

Basic data processing was carried out using the CXC pipeline software packages available in CIAO v4.7. Each ACIS observation was handled separately, and the latest calibration files (CALDB v4.6.7) were applied using the `chandra_repro` script to produce new and up-to-date level-1 events files. We used the `acis_process_events` tool to remove the standard pixel randomization, and streak events, bad pixels and cosmic rays were removed by setting STATUS = 0. Events files were screened using a typical grade set (grade = 0, 2, 3, 4, 6) and background flares that were detected at 3σ above the mean count rate were removed using `lc_clean` to create new Level-2 events files. Subsequent spectral images were constructed for each ObsID from the Level-2 events. Aspect histograms were constructed using the `aspecthist` tool available in the CHAV software package. The aspect histograms were then convolved with the appropriate ACIS chip-map to generate the necessary exposure maps. The total exposure in good-time intervals are provided in Table 2. The median exposure time was $\sim$40 ks. Exposure corrected images in the 0.3–5keV band were constructed from the band images and exposure maps (see Figure 2). For those sources with multiple *Chandra* ObsIDs, the events images and exposure maps were combined into single contiguous images using the method outlined in Goulding et al. (2012). However, this merging was performed for presentation purposes only. All subsequent spectral extraction and spectral fitting (see below) was performed on the individual ObsID data.

In-depth studies of the Local Group galaxies have shown that the X-ray emission detected in these systems is a complex mixture of emission arising from a diffuse thermal plasma (the hot ISM), low-mass X-ray binaries (LMXBs), active binaries (ABs), cataclysmic variables (CVs), and mass accretion onto the supermassive black hole at the galaxy center (Fabbiano 2006; Revnivtsev et al. 2007; Bogdán & Gilfanov 2008). Indeed, observations of M31 and M32 have resolved the full population of LMXBs to provide a more complete view of the expected contributions to the total X-ray emission from the unresolved stellar systems (e.g., Gilfanov 2004; Boroson et al. 2011). To remove a significant fraction of the X-ray emission due to those LMXBs that are resolved as point-sources (typically 5–10 per galaxy) within our data, we use the CIAO tool `wavdetect` to detect and subsequently mask these stellar systems. Point sources were detected with `wavdetect` in the 0.3–7 keV band with a significance threshold of 10^{-7} using native pixel wavelet scales of 1, $\sqrt{2}$, 2, $2\sqrt{2}$ and 4. After source detection, the point source position was iterated up to five times to more accurately determine the centroid. The region covered by 90% of the predicted encapsulated energy by a point-source at 1.5 keV at the appropriate chip position of the source was then masked from further spectral analyses. In the case of the presence of an active galactic nucleus, this masking procedure included the central region of the galaxy.

3.2. *Spectral Extraction*

The hot X-ray emitting gas extends to tens to hundreds of times the optical extent of the galaxy. As such, we choose to adopt two different regions for extracting the diffuse gas emission. The first (smaller) region is a circular aperture matched to the optical size of the galaxy, specifically centered at the peak of the X-ray emission with radius equal to one effective radius of the galaxy ($r = R_e$; see section 2.2; e.g., Diehl & Statler 2007). This particular methodology allows a more direct measurement of the X-ray gas associated with the galaxy properties. The second (larger) extraction region follows the more typical methodology for analyzing diffuse X-ray emission. We extract all of the X-ray photons out to where the diffuse component becomes equal to the background emission within the X-ray observation (e.g., Boroson et al. 2011; Bogdán et al. 2012a,b; Kim & Fabbiano 2015).[3]

In several cases, the diffuse emission associated with the galaxy, group and/or cluster filled a significant fraction of the ACIS chip, and hence prevented a direct extraction of the background photons from the on-source chip. Hence, we chose to adopt three separate methods to provide the best appropriate estimate of the X-ray background within the observation: First, and where possible, we used extraction regions twice the area of the source aperture on the same chip (typically S3) as the source, assuming these were free from diffuse source emission. Second, multiple regions from the S1 (i.e., the second back-illuminated chip on the ACIS instrument) chip were extracted, assuming this chip was also free

[3] For NGC 4472 and NGC 4649, the diffuse emission, as measured within a circular aperture, extended beyond the coverage of a single chip. Hence, for the full aperture diffuse X-ray emission we adopt the previous lower-limit measurements of Diehl & Statler (2007).

TABLE 2
X-ray Data & Properties

Common Name	Date	Obs-ID	t_{exp}	T_{X,gas,R_e}	f_{X,gas,R_e}	L_{X,gas,R_e}	$\chi^2_{R_e}$ (d.o.f.)	$T_{X,gas,tot}$	$f_{X,gas,tot}$	$L_{X,gas,tot}$	χ^2_{tot} (d.o.f.)
			(ks)	(keV)	(erg s^{-1} cm^{-2})	(10^{40} erg s^{-1})		(keV)	(erg s^{-1} cm^{-2})	(10^{40} erg s^{-1})	
(1)	(2)	(3)	(4)	(5)	(6)	(7)	(8)	(9)	(10)	(11)	(12)
NGC0057	2008-10-29	10547	9.9	0.92 ± 0.05	-12.548 ± 0.019	19.8	185.6 (171)	0.92 ± 0.05	-12.529 ± 0.025	20.6	339.7 (378)
NGC0315	2003-02-22	4156	55.0	0.66 ± 0.04	-12.574 ± 0.089	16.2	470.3 (327)	0.57 ± 0.05	-12.192 ± 0.042	38.0	563.1 (433)
NGC0383	2000-11-06	2147	44.4	0.82 ± 0.05	-13.091 ± 0.021	5.0	259.1 (226)	1.09 ± 0.09	-12.861 ± 0.048	8.4	495 (458)
NGC0410	2004-11-30	5897	2.6	0.80 ± 0.06	-12.194 ± 0.027	39.6	141.1 (108)	0.86 ± 0.06	-12.129 ± 0.031	45.2	204.2 (255)
NGC0499	2009-02-12	10536	18.4	0.83 ± 0.05	-12.512 ± 0.015	18.2	208.4 (183)	0.75 ± 0.04	-11.561 ± 0.006	160.2	548.6 (454)
NGC0507	2000-10-11	317	26.9	1.13 ± 0.05	-12.173 ± 0.081	39.7	670.7 (400)	1.29 ± 0.04	-11.452 ± 0.070	205.9	669.1 (455)
NGC0533	2002-07-28	2880	37.6	0.92 ± 0.04	-11.998 ± 0.056	75.5	771.0 (330)	1.11 ± 0.09	-11.802 ± 0.063	114.6	1116.1 (454)
NGC0547	2007-09-07	7823	64.8	0.74 ± 0.05	-12.998 ± 0.015	7.5	431.3 (281)	0.70 ± 0.05	-12.834 ± 0.018	9.6	1078.3 (458)
NGC0708	2006-11-20	2215,7921	139.5	1.56 ± 0.04	-11.312 ± 0.080	254.5	6687.6 (982)	1.91 ± 0.07	-10.915 ± 0.011	693.0	4833.6 (908)
NGC0741	2001-01-28	2223	30.3	0.80 ± 0.04	-12.523 ± 0.015	19.7	302.9 (243)	1.04 ± 0.13	-12.301 ± 0.017	32.7	704.3 (454)
NGC0777	2004-12-23	5001†	10.0	0.96 ± 0.05	-12.106 ± 0.017	49.9	216.7 (158)	0.79 ± 0.04	-11.689 ± 0.011	127.7	427.7 (398)
NGC1129	2009-11-05	11717†,12017†	79.9	2.91 ± 0.36	-11.499 ± 0.035	206.7	579.6 (442)	4.23 ± 0.16	-10.158 ± 0.026	4542.5	665.4 (454)
NGC1132	2003-11-16	801,3576	53.7	1.01 ± 0.04	-12.530 ± 0.010	32.9	535.6 (296)	1.09 ± 0.10	-11.923 ± 0.068	136.1	988.2 (454)
NGC1600	2002-09-20	4283,4371	53.5	1.05 ± 0.04	-12.560 ± 0.017	12.6	1074.7 (707)	1.10 ± 0.05	-12.457 ± 0.020	17.0	1537.6 (908)
NGC1700	2000-11-03	2069	42.8	0.45 ± 0.05	-12.938 ± 0.015	4.1	389.2 (328)	0.34 ± 0.04	-12.586 ± 0.018	9.2	207.8 (104)
NGC2340	2005-02-04	5898	1.9	0.85 ± 0.10	-12.679 ± 0.055	20.2	73.4 (75)	1.15 ± 0.15	-12.687 ± 0.124	20.0	213.0 (240)
NGC2783	2005-01-13	5789	17.9	0.81 ± 0.09	-13.323 ± 0.038	5.7	242.8 (180)	0.82 ± 0.08	-13.297 ± 0.055	6.2	391.9 (375)
NGC2832	2005-01-02	5904†	3.0	1.16 ± 0.09	-12.292 ± 0.060	67.6	70.5 (95)	1.13 ± 0.12	-12.245 ± 0.081	75.3	359.8 (399)
NGC3209	2005-02-17	5792	21.7	0.68 ± 0.08	-13.331 ± 0.033	4.7	189.1 (159)	0.70 ± 0.06	-13.245 ± 0.039	6.1	472.0 (440)
NGC3842	2003-01-24	4189	47.5	1.01 ± 0.05	-13.212 ± 0.032	7.2	437.5 (272)	1.32 ± 0.11	-13.009 ± 0.056	11.6	1065.1 (454)
NGC4073	2002-11-24	3234	30.0	1.54 ± 0.05	-11.806 ± 0.011	152.4	773.6 (318)	1.85 ± 0.04	-11.120 ± 0.070	760.1	1262.1 (454)
NGC4472	2011-02-21	12888,12889	294.9	0.94 ± 0.04	> -11.610	>16.7	14851.0 (908)	>1.25	> -11.594	>83.2	-
NGC4555	2003-02-04	2884	30.0	0.91 ± 0.04	-12.817 ± 0.014	20.2	323.8 (210)	1.06 ± 0.05	-12.509 ± 0.020	39.8	600.2 (449)
NGC4649	2011-02-24	12976	101.0	0.89 ± 0.04	-11.642 ± 0.002	7.5	1161.6 (445)	0.90 ± 0.04	> -11.507	>12.9	998.4 (454)
NGC5129	2006-05-14	6944,7325	46.8	0.87 ± 0.05	-12.695 ± 0.015	28.0	585.0 (373)	0.92 ± 0.04	-12.163 ± 0.011	95.0	937.6 (906)
NGC5322	2006-08-20	6787	13.8	0.44 ± 0.08	-13.444 ± 0.073	0.4	146.3 (147)	0.44 ± 0.06	-13.433 ± 0.068	0.5	157.4 (148)
NGC5353	2014-03-31	14903	40.3	0.73 ± 0.05	-12.744 ± 0.015	3.5	357.9 (253)	0.66 ± 0.04	-12.362 ± 0.013	8.8	553.0 (454)
NGC6482	2002-05-20	3218	19.3	0.89 ± 0.04	-11.984 ± 0.083	48.1	429.0 (202)	0.71 ± 0.04	-11.676 ± 0.072	95.1	565.8 (451)
NGC7052	2002-09-21	2931	9.6	0.56 ± 0.06	-12.535 ± 0.023	17.6	245.6 (157)	0.61 ± 0.06	-12.439 ± 0.024	20.9	539.6 (351)
NGC7265	2006-06-07	7058†	5.0	0.55 ± 0.10	-12.759 ± 0.066	14.3	70.0 (76)	0.86 ± 0.10	-12.092 ± 0.052	66.4	292.7 (326)
NGC7618	2007-09-08	7895	34.1	0.99 ± 0.04	-12.301 ± 0.011	35.2	479.1 (242)	0.83 ± 0.04	> -11.747	>124.8	1825.8 (454)
NGC7619	2003-09-24	3955	37.5	0.84 ± 0.04	-12.308 ± 0.007	17.2	648.1 (309)	0.87 ± 0.04	-11.986 ± 0.007	36.0	1060.9 (454)
NGC7626	2001-08-20	2074†	26.7	0.69 ± 0.06	-12.862 ± 0.026	4.9	220.5 (220)	0.71 ± 0.05	-12.579 ± 0.026	9.2	486.9 (454)

Notes:- [1]Common galaxy name; [2]*Chandra* X-ray observation date; [3]*Chandra* observation identification numbers for ACIS-S observations (†: ACIS-I); [4]Cleaned exposure time in kilo-seconds; [5]Temperature of best-fit `APEC` model for photons extracted within R_e (uncertainties include an additional systematic for the choice of the `APEC` model); [6]0.3–5keV X-ray flux of best-fit model for photons extracted within R_e; [7]Derived 0.3–5keV gas X-ray luminosity within R_e; [8]Chi-squared value from model fitting for R_e aperture, and the number of degrees of freedom are given in parentheses; [9]Temperature of best-fit `APEC` model for photons extracted out to background-level of observation (uncertainties include an additional systematic for the choice of the `APEC` model); [10]0.3–5keV X-ray flux of best-fit model for photons extracted out to background-level of observation; [11]Derived 0.3–5keV gas X-ray luminosity for photons extracted out to background-level of observation; [12]Chi-squared value from model fitting for the large aperture, and the number of degrees of freedom are given in parentheses.

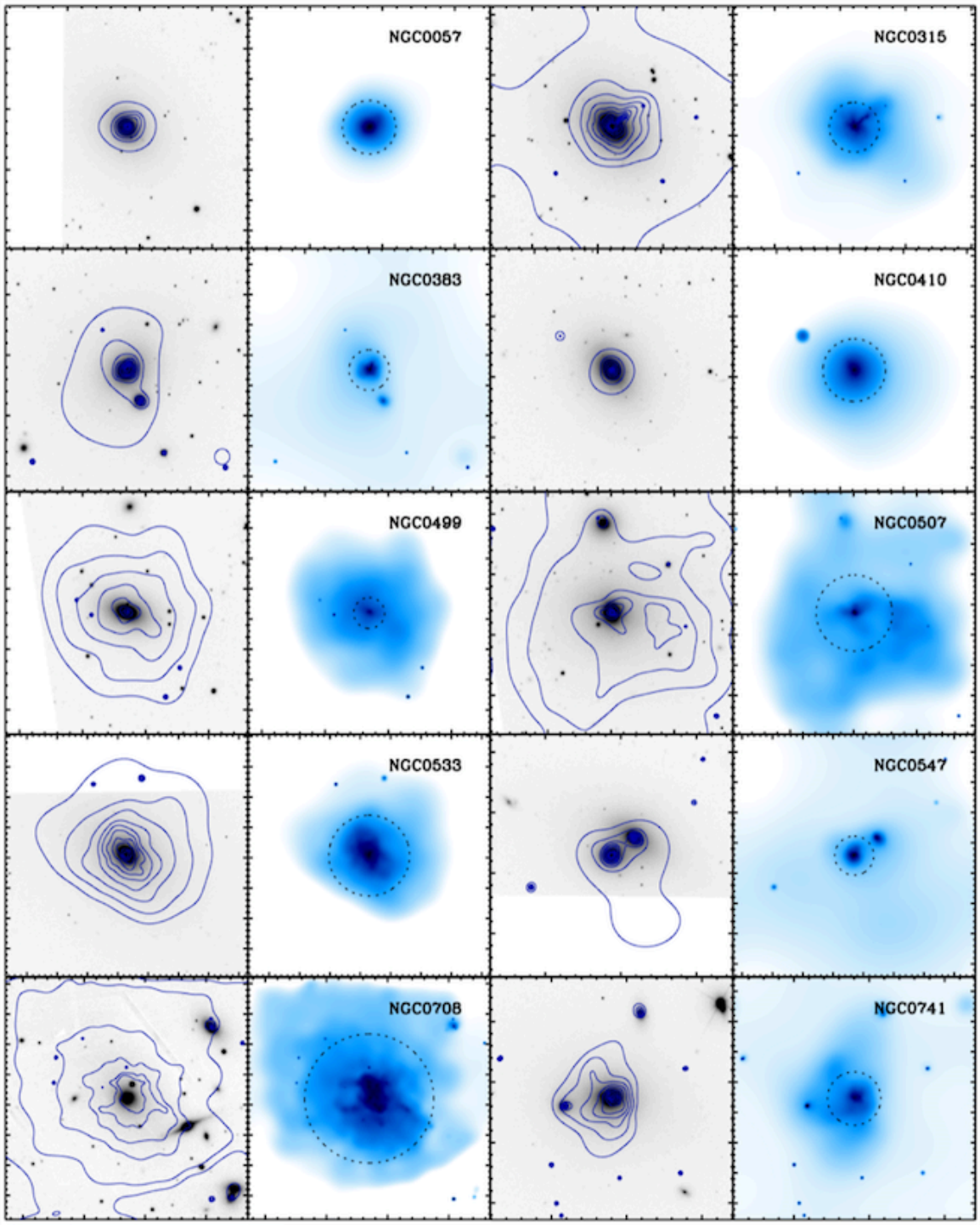

FIG. 2.— 4×4 arc-minute cutouts of the MASSIVE galaxies with publicly available archival *Chandra* X-ray observations performed with the ACIS instrument. Left column shows the optical *i*-band SDSS DR12 Atlas image, logarithmic X-ray contours are overlaid in solid blue. *g*-band PANSTARRS images are shown for NGC 708, 1600, 2340, 6482, 7052, 7265 and 7618 as they do not fall within the SDSS survey footprint. The logarithm of the adaptively-smoothed, vignetting and exposure-corrected *Chandra* ACIS-S (NGC 1129: ACIS-I) images are shown to the right of the optical images. Dashed circles represent one effective radius derived from optical and near-infrared imaging.

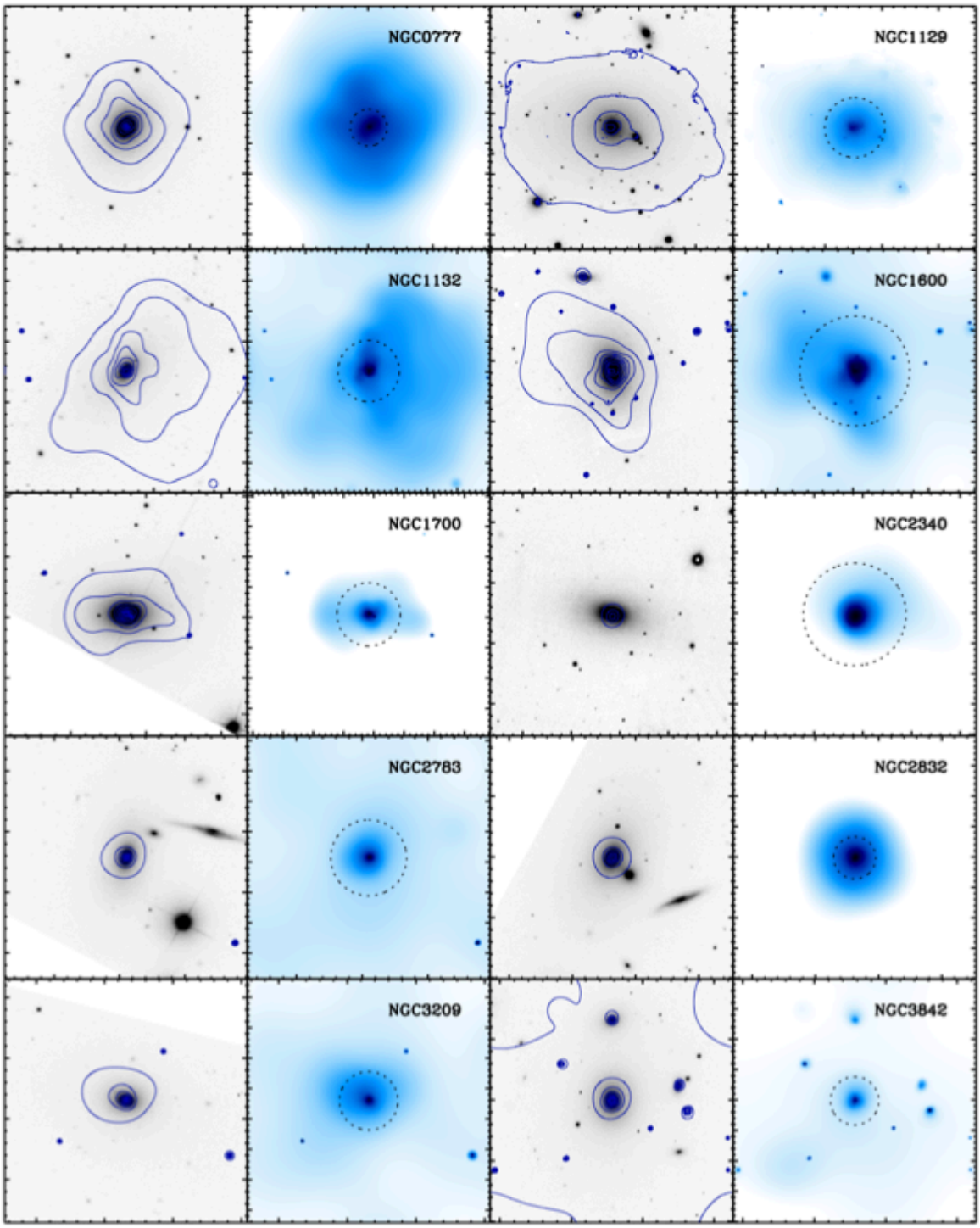

Fig. 3.— Figure 2 continued...

from diffuse emission. Third, we harnessed the appropriate stowed *Chandra* observations normalized to the hard energy (10–12 keV) count rates of the relevant ObsIDs to extract background spectra from the same regions used for the full aperture source spectra. These 'stowed' observations are a set of blank-sky observations performed with *Chandra* that provide the appropriate ACIS background for a set of ObsIDs.[4]

Spectra were extracted from source and background regions using the `specextract` tool available in CIAO, and ancillary response and redistribution matrices were constructed during the spectral extraction. Extracted spectra were grouped to contain one count per bin. For sources with weak jet structures (i.e., those not already excluded due to pile-up effects) visible in the exposure-corrected images, we additionally masked the jet region

[4] See `http://cxc.harvard.edu/ciao/threads/acisbackground/` for further details.

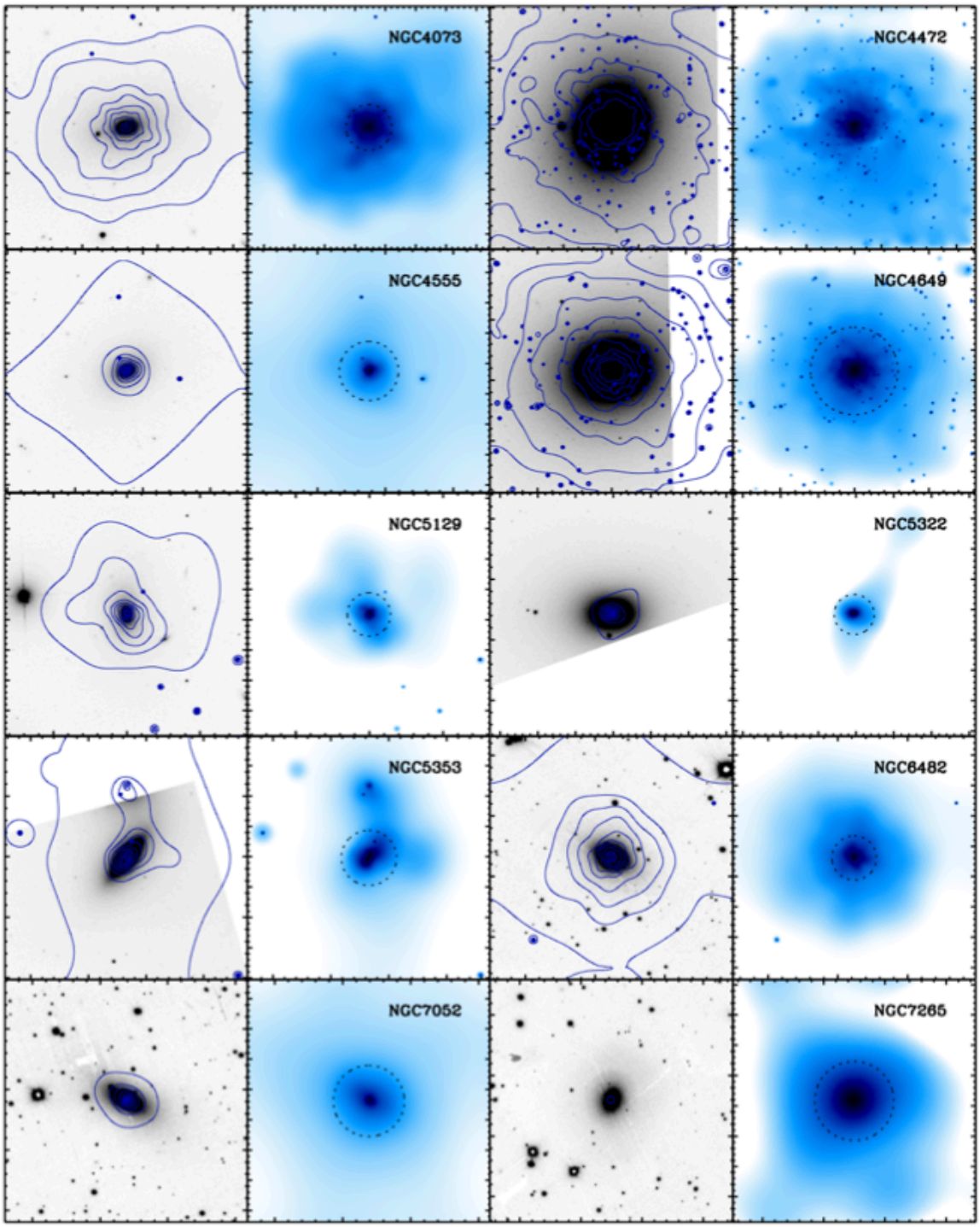

FIG. 4.— Figure 2 continued...

using a rectangular box during spectral extraction oriented along the direction of the jet axis.

As noted previously, the high-energy emission observed in elliptical galaxies arises due to several phenomena. We followed Boroson et al. (2011) to characterize the dominant emission sources contributing to the X-ray spectroscopy. After the direct subtraction of the bright LMXB population, we model the diffuse hot gas as a thermal plasma (`APEC`) component, with the metallicity fixed at solar; for the remaining LMXB population that lies below the sensitivity threshold of the X-ray observations we use a thermal Bremsstrahlung model fixed to a temperature of 7 keV; a powerlaw component with $\Gamma = 1.6$ is used to model the AB/CV population; and for those galaxies with obvious nuclear activity (i.e., significant emission at $E > 4$ keV), we include an absorbed powerlaw with Γ allowed to vary within the fitting. Additionally, we include a photoelectric absorption component fixed to the Galactic column density ($N_{\rm H}$) along the line of sight to each

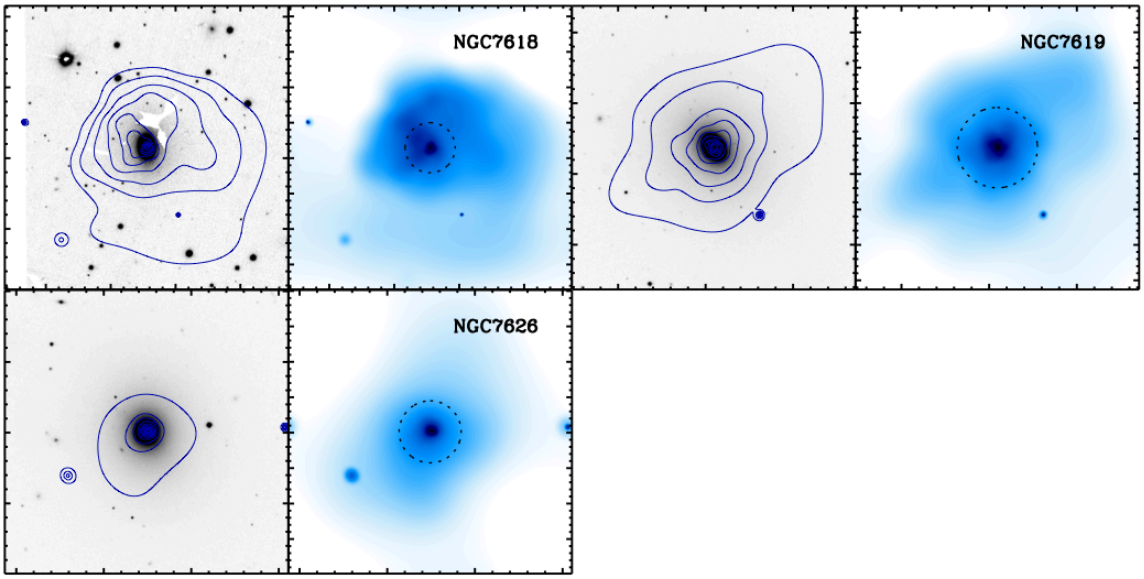

Fig. 5.— Figure 2 continued...

source. In XSPEC language our adopted model is given as `phabs×(apec+bremss+pow+[phabs×pow])` (e.g., Boroson et al. 2011; Kim & Fabbiano 2015). During spectral fitting we limit the fitted energy range to $E = 0.3$–7 keV, which is typical for *Chandra* ACIS observations. Typical reduced χ^2 statistics for the model fits were in the range 0.8–2.5 (see columns 8 and 12 of Table 2). Some of the fits are formally not acceptable, this is particularly evident for sources with large numbers of detected photons. Based on testing of our assumed model and comparison to previous literature (e.g., Diehl & Statler 2008; Kim & Fabbiano 2015; see also Appendix in this work), we determine that a combination of our assumed fixed solar metallicity (see below), the requirement of a second temperature component in some sources, as well as marginal systematic differences in the *Chandra* calibration at low energies, drive the large chi-squared values in these sources. However, we find within this subset of high-count sources that while the fit may be formally improved with a more complex model that is fit in a restricted energy range, it has no effect on our measured $T_{\rm gas}$ or $f_{\rm X,gas}$, particularly within the $1R_e$ apertures, which are adopted throughout Section 4.

In the majority of cases, the `powerlaw` model, motivated to represent the AB/CV population, was substantially sub-dominant compared to the other emission components. However, given the relatively high stellar mass (high K-band luminosity) of the MASSIVE galaxies, it should not be surprising given that the expected X-ray luminosity for the AB/CV population is over an order of magnitude lower than the gas components measured here based on the typical L_X/L_K ratio for the AB/CV population located in Local Group galaxies (e.g., Revnivtsev et al. 2007). For those sources with multiple observations, the spectra were not combined into one single spectrum, but instead the spectra were modeled simultaneously. The final unabsorbed X-ray fluxes at $E \sim 0.3$–5 keV ($f_{\rm X,gas}$), derived luminosities ($L_{\rm X,gas}$), and temperatures ($T_{\rm gas}$) quoted in Table 2 are for the `APEC` thermal gas component derived from the X-ray fitting process for the emission detected within $r = R_e$ and $r < R_{\rm bkg}$.

While our assumption of a solar metallicity for the thermal component allows a homogeneous temperature measurement (i.e., one that is not subject to a degeneracy between abundance and temperature in the low-count regime), it may not provide the most accurate description of the data for some sources. To test for a systematic bias in the measured temperature and normalization (flux) of the `APEC` component, we re-fit the 23 MASSIVE galaxies that had >1000 counts in their X-ray spectra, but with the metallicity as a free parameter during the fitting process. The metallicities for these sources were found to be in the range, 0.1–2.8 solar consistent with previous analyses (e.g., Buote 2000). However, for the majority of the systems, we found that the metallicity was still poorly constrained, and often consistent with solar metallicity. Particularly for the highest $T_{\rm gas}$ sources, we found that allowing the gas metallicity to vary within the fit improved the overall χ^2 significantly ($\Delta\chi^2 \sim 5-10\%$). However, with the exceptions of NGC 708 and NGC 4073, within R_e, a fixed solar metallicity had no significant impact on the temperature or flux at the $< 3\%$ level. For NGC 708 and NGC 4073, we found an increase in the observed temperature of ~ 0.2 keV, and a $\sim 10\%$ decrease in the flux, though neither of these have any significant impact on our results.

In order for us to better compare to previous literature, we also tested for underlying systematics in our determination of the luminosity and temperature measured through the use of `APEC` compared to a `MEKAL` model (for example) which has also been used. `APEC` now includes the most up-to-date atomic libraries with the most recent photoionization and recombination rates for a variety of elements while the `MEKAL` model is no longer maintained. Indeed, we determine that, on average, the plasma temperatures measured for the MASSIVE sample with a `MEKAL` model are $\sim$ 7–12% lower than those found us-

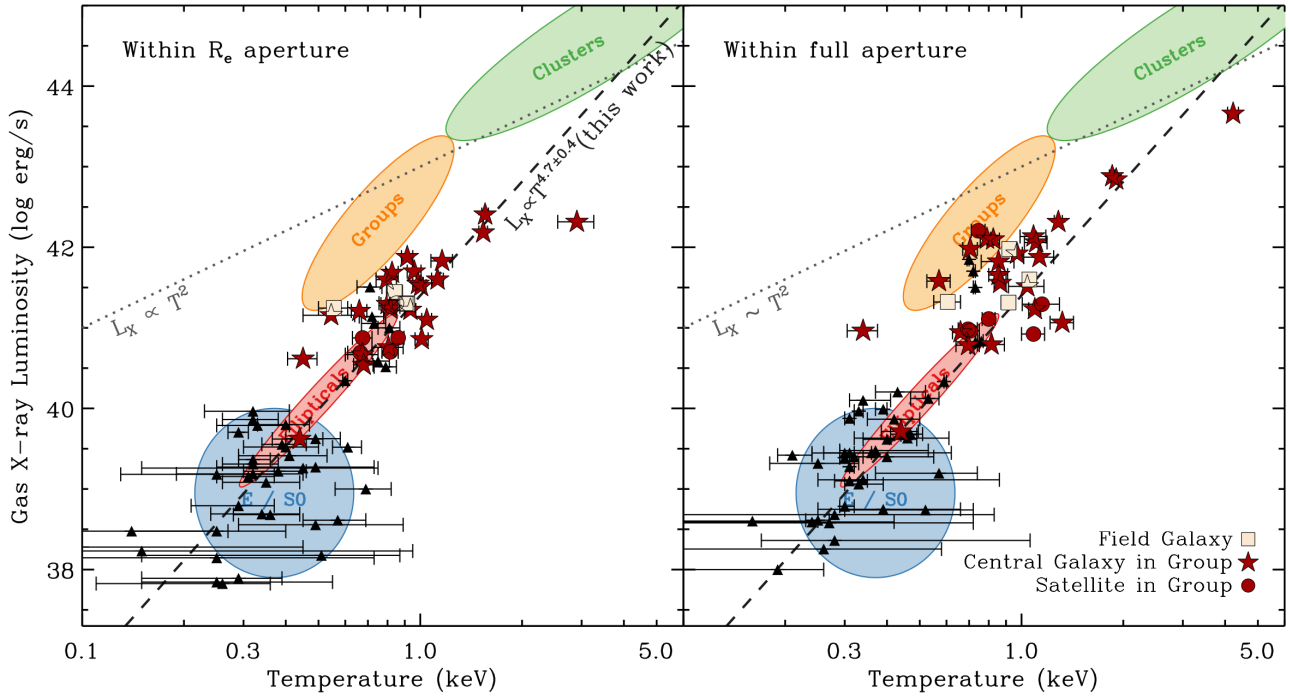

FIG. 6.— **Common:** Logarithm of 0.3–5.0 keV X-ray luminosity of the diffuse gas APEC component versus the X-ray temperature of the gas (in units of keV). Stars represent those MASSIVE galaxies that are determined to lie at the center of their group environment in the catalog of Crook et al. (2007), satellite galaxies in groups are shown with circles, and field galaxies (≤ 3 neighbors) are shown with light-shaded square symbols. Black triangles represent the ATLAS^{3D} comparison sample (see Section 2.5 and Appendix). Background ellipses are reproduced and adapted from Kim & Fabbiano (2015). These regions are used to represent the previously observed positions of the (coreless/disky) E/S0 galaxies (blue shading), core-dominated/slow-rotating ellipticals (red shading), hot gaseous emission associated with groups (orange shading) and clusters (green shading). The dashed line shows our best-fit relation ($L_{\rm X,gas} \propto T^{4.7\pm0.4}$; $\epsilon_{\rm intrinsic} \sim 0.42-0.50$ dex) to the MASSIVE and ATLAS^{3D} galaxies with constrained $T_{\rm gas}$ measurements performed within R_e apertures. The dotted line represents the self-similar $L_{\rm x,gas} \sim T^2_{\rm gas}$ relation. In general, the uncertainties in the X-ray luminosities are small (e.g., see Table 2 and Figure 7), and are not shown in the figure for presentation purposes only. **Left:** X-ray luminosity and gas temperature measured within one effective optical radius of the galaxy **Right:** X-ray luminosity and gas temperature measured out to large radii where the X-ray emission associated with the galaxy/halo meets the X-ray background level in the observation.

ing the more recent APEC model. However, we found no appreciable difference between the fluxes produced using these two models. Within our MASSIVE X-ray sample, there are 14 sources in common with the analyses of the structure of the hot ISM in ellipticals of Diehl & Statler (2008). Adopting our above method with a MEKAL model produces perfectly consistent temperatures for these 14 sources, despite Diehl & Statler adopting an extraction radius that was a factor ~ 3 larger than that considered here. However, a comparison between the most recent APEC model and that used in Diehl & Statler, produced temperatures that were consistent only to within a factor $\sim$1.1 of the quoted temperatures, which is several sigma larger than the statistical uncertainties found during the fitting process. We thus adopt an additional 10% systematic uncertainty into the measured temperatures with APEC to allow us to more readily compare to the previous measured values for some of these sources derived using MEKAL or older ionization tables used with previous versions of the APEC model.

Finally, we also tested for the presence of a systematic bias in our flux and temperature measurements within R_e due to the assumption of a single homogeneous gas temperature. For larger radius measurements, well-studied galaxies are known to have radial temperature gradients due to the large scale halo. Given much of the following analyses focus on the X-ray measurements within R_e it is important to test whether our $T_{\rm gas}$ measurements are biased by line-of-sight gas, associated with the halo, rather than the central galaxy. We refit each of the R_e aperture X-ray spectra by including an additional APEC component with fixed solar metallicity. For the majority of the MASSIVE galaxies (28/33), we found no significant improvement in the calculated χ^2 value (F-test reveals < 0.95 confidence). Five of the MASSIVE galaxies showed a significant improvement in the fit. We found that within the R_e aperture, the dominant APEC component had a temperature consistent with that measured with the single temperature model. We determined that the overall improvement to the fit was driven by a sub-dominant higher temperature component, consistent with that expected from line-of-sight emission. The one exception was NGC 708, where we determined that a single temperature model was insufficiently fitting two distinct temperature gas components. The two temperature model for NGC 708 has $T_{\rm gas,Re,1} \sim 2.0\pm0.1$ keV and $T_{\rm gas,Re,2} \sim 1.1\pm0.1$ keV, where the cooler component is a factor $5-7\times$ fainter than the hot component. For consistency, with the remainder of the MASSIVE sample, we adopt the single temperature model measurement. Overall, we conclude that a single temperature model provides an accurate measurement of the dominant X-

ray gas properties within R_e with no systematic bias.

4. RESULTS

4.1. *The X-ray properties of the high mass early-type galaxy population*

Two of the most fundamental measurables of the X-ray emitting thermal ISM are its luminosity and temperature. In Figure 6 we present the X-ray luminosity at 0.3–5 keV versus temperature measured for the thermal gas component of the 33 sources in the MASSIVE X-ray galaxy sample, along with the ATLAS^{3D} sample described in detail in Section 2.5 (also see Appendix). To fully harness the available X-ray data and build the most coherent picture of the hot gas properties of early-type galaxies, we present two measurements of $L_{\rm X,gas}$ and $T_{\rm gas}$: (1) measured within an aperture defined by the optical radius of the galaxy ($r = R_e$) to accurately characterize the X-ray emission directly associated with the galaxy and the galaxy potential; and (2) measured in large apertures out to radii where the source X-ray photons approximate the observed X-ray background to provide a good measure of the total X-ray luminosity of the gas associated with the galaxy and the galaxys wider environment. See Section 3.2 for further details.

With the exception of NGC 5322, all of the MASSIVE galaxies have $L_{\rm X,R_e} \gtrsim 10^{40}\,{\rm erg\,s^{-1}}$ and hence, can be considered hot-gas–rich systems. The full MASSIVE X-ray galaxy sample covers a wider range in gas temperature ($T_{\rm gas} \sim 0.3 - 4$ keV) than previously observed for individual early-type galaxies. Although the majority (27/33; ∼80%) exhibit temperatures of $T_{\rm gas} \sim 0.5 - 1.2$ keV, this is the poorly-sampled region of $T_{\rm gas}$-space in previous studies. The observed temperatures are almost independent of the aperture radius used to extract the source photons.

On average, we observe a shift of ∼0.1 dex towards higher $T_{\rm gas}$ in the large aperture measurements, suggesting that the inner X-ray halos of massive galaxies are systematically (marginally) cooler than the larger scale gas. We tested this systematic difference between the temperatures within R_e and out to $R_{\rm tot}$ by additionally performing an X-ray spectral analysis that excluded the photons from the inner R_e aperture for the 13 objects that had >1000 counts within the annulus ($R_{\rm tot} - R_e$) region[5]. For seven of the sources, the temperature measurements within the annulus were entirely consistent with the total measurements performed in the large aperture. One source, NGC 6482, showed a decrease in the temperature within the annulus of 0.1 keV (∼14%) compared with the large $R_{\rm tot}$ aperture measurement. This is consistent with our measurement that $T_{\rm gas}$ is higher at smaller radii, i.e., $T_{\rm gas,R_e} > T_{\rm gas,R_{tot}}$. The annulus $T_{\rm gas}$ measurements for five of the most luminous objects were ∼0.1–0.2 keV higher compared with the large aperture measurement. This suggests that at high luminosities and high temperatures, our $T_{\rm gas}$ measurements within $R_{\rm tot}$ may be biased marginally low due to the inclusion of the cooler gas within R_e. This in turn would suggest a marginally larger discrepancy between the inner gas temperature and the temperature of the wider halo than the ∼ 0.1 dex we calculate above.

We perform a linear regression (for the combined ATLAS^{3D} and MASSIVE samples) using a Bayesian approach to simultaneously include the uncertainties in both $L_{\rm X,gas}$ and $T_{\rm gas}$ using the IDL routine LINMIX_ERR (Kelly 2007). Specifically, we fit the data for the galaxy-scale (R_e) aperture for all objects with constrained measurements. We find $\log L_{\rm X,gas} = (41.4 \pm 0.1) + (4.7 \pm 0.4)\log T_{\rm gas}$, with a well-constrained intrinsic scatter of ∼0.42–0.50 dex. The quoted uncertainties are derived from the central 67% of the posterior draws. The data is characterized by a single powerlaw fit with a reduced χ^2 (χ^2/d.o.f.) of 441.2/72 = 6.1. This large reduced chi-squared value is no doubt driven by the amplitude of the intrinsic scatter (0.42–0.50 dex) present within the data. A two-powerlaw model marginally improves the fit with $\Delta\chi^2 \sim 18.6$ for two additional free parameters. An F-test between the models results in an acceptance of the new 2 power law model with a confidence of only 0.78 (i.e., $< 2\sigma$). Thus, we find no significant evidence to reject a single power law.

The $L_{\rm X,gas} - T_{\rm gas}$ relation calculated from the full aperture measurements has a consistent slope, but with considerably higher scatter (∼1.0 dex). This larger scatter is likely due to the inclusion of gas from the larger-scale environment for the MASSIVE galaxies. For the R_e aperture measurements, the scatter about the $L_{\rm X,gas} - T_{\rm gas}$ relation is relatively constant over a wide range in $L_{\rm X,gas}$ and $T_{\rm gas}$. Thus, despite the early-type systems considered here covering a wide-range in stellar mass, velocity-dispersion, and wide-scale environment, the intrinsic scatter remains remarkably constant at ∼ 0.5 dex. Furthermore, we also find that there appears to be no dependence of the scatter about the $L_{\rm X,gas} - T_{\rm gas}$ relation with the slow/fast-rotators (core/power-law) galaxy morphologies or the radio power of the central black hole.

Within $1R_e$, the $L_{\rm X,gas}$ for MASSIVE galaxies in poor groups ($N_{\rm neighbors} \leq 5$) versus those in rich groups ($N_{\rm neighbors} > 5$) are also extremely similar, median $L_{\rm X,poor} \sim 2.0 \times 10^{41}\,{\rm erg\,s^{-1}}$ and $L_{\rm X,rich} \sim 1.7 \times 10^{41}\,{\rm erg\,s^{-1}}$, respectively. However, when we consider $L_{\rm X,gas}$ measured to large radii, we find a systematic increase in $L_{\rm X,gas}$ of a factor $\sim 3 - 5$ for the rich group galaxies. Indeed, for the rich-group systems in MASSIVE and ATLAS^{3D}, we show in Figure 6b that these sources occupy a similar locus in $L_{\rm X,gas} - T_{\rm gas}$ to that expected for group gas halos. Furthermore, we find that the scatter in the $L_{\rm X,gas}$–$T_{\rm gas}$ relation increases significantly (∼ 0.95 dex) for the large aperture measurements. Taken together, this suggests that the increase in $L_{\rm X,gas}$ for large aperture measurements is due to significant contributions from the group/cluster gas as the galaxy X-ray emitting halo extends into the large-scale environment within which the galaxy is embedded.

Our main conclusions about the $L_{\rm X,gas} - T_{\rm gas}$ relation are as follows. First, we see that over a very wide range in galaxy mass, early-type galaxies obey a single power-law relation between these two parameters when attention is restricted to the gas within the effective radius. We argue that an aperture matched to the host stellar light is the most physically motivated way to compare these systems. Second, from the data in hand, the intrinsic scatter within this relation is ∼ 0.5 dex across the en-

[5] We did not perform this annular analysis on NGC4472, NGC4649 and NGC7618 as the X-ray halos of these galaxies are extended well beyond the Chandra field of view

tire relation with no dependence on galaxy mass (L_K). Third, when we focus on the galaxy-scale aperture measurements, the slopes are found to be consistent (within 1 sigma) for both the fast-rotating and slow-rotating galaxies. We further determine that for the high mass galaxies, there is no distinction between the X-ray luminosities (or temperatures) of galaxies based on their locale in the large-scale environment. Specifically, we show that isolated/field galaxies (with $N_{\rm neighbors} \leq 3$) and those systems considered to be central or satellite members of their respective galaxy groups, all occupy the same locus of the $L_{\rm X,gas} - T_{\rm gas}$ relation; there is no evidence for an offset towards high-$L_{\rm X,gas}$ for central galaxies in groups.

4.1.1. *Comparison with Previous Work*

To date, the largest study of early-type systems with high-quality X-ray observations was presented in Kim & Fabbiano (2015). By focusing on the ATLAS$^{\rm 3D}$ sample, Kim & Fabbiano made a comprehensive effort to link the stellar and hot gas properties of a well-defined, volume-limited sample of early-type galaxies. The main result from Kim & Fabbiano is illustrated schematically in Figure 6. They argue that low-mass, fast-rotating, power-law ellipticals and S0 galaxies occupy a poorly-defined region of $L_{\rm X,gas} - T_{\rm gas}$ parameter space, with $L_{\rm X,gas} \sim (0.1-10) \times 10^{39}\,{\rm erg\,s^{-1}}$ and $T \sim 0.2-0.6$ keV, as illustrated schematically by the blue circle in Figure 6 (see also their Figs. 4 and 8). By contrast, when they focus on the core galaxies in ATLAS$^{\rm 3D}$ that are isolated field galaxies, they seemingly form a tight ($\sim$0.2 dex) relation in $L_{\rm X,gas} - T_{\rm gas}$, following a steep slope of ~ 4.5 (the red ellipse). However, due to the limitied 40 Mpc volume of ATLAS$^{\rm 3D}$, their survey is vastly dominated by relatively low-mass fast-rotating power-law early-type galaxies.

By adding a much larger sample of high-mass galaxies, we first confirm (within 1σ) the slope of $\sim$4.5 measured by Kim & Fabbiano, although we argue that it is only robustly determined when considering the gas within R_e. If we consider the MASSIVE galaxies in isolation, we measure a slope of 4.5 ± 0.2 for measurements performed within R_e.[6] By contrast, the slope becomes poorly determined if we consider the measurements in the full aperture, owing to the significant scatter in $L_{\rm X,gas}$ likely due to mixing and contamination from gas associated with the group/cluster halo. In contrast to the previous results of Kim & Fabbiano, we do not find evidence that the detailed properties of the early-type galaxies (e.g., fast/slow rotation; radio power at 1.4 GHz; large scale halo mass) play a significant role in either the slope or the scatter in the $L_{\rm X,gas} - T_{\rm gas}$ relation (see Section 4.1), when the X-ray measurements are performed within physically motivated R_e apertures. Therefore, we deduce that an $L_{\rm X,gas} \propto T_{\rm gas}^{\sim 4.5}$ relation can be considered universal across all early-type galaxies when the X-ray properties are measured on scales set by the stellar light.

Our different lines of investigation strongly suggest that the X-ray properties of elliptical galaxies can be readily determined by considering only their X-ray emission within $1R_e$. On these smaller scales, the gas temperature may be primarily set by the sub-halo of the galaxy being at (or close to) virial equilibrium with bulk gas motions due to temperature diffences (so-called cooling flows) possibly playing a secondary role[7]. The single sequence observed in $L_{\rm X,gas} - T_{\rm gas}$ for all early-type galaxies suggests that, despite the vastly different mass and gravitational scales, the gas $T_{\rm gas}$ and $L_{\rm X,gas}$ of the inner $10-30$ kpc of a galaxy group or cluster are set solely by the properties of the galaxy residing at its center, and not by the wider environment. Overall, our analysis of the X-ray luminosity and temperature distributions of elliptical galaxies suggests a smooth and uniform scaling of the intrinsic X-ray properties between low-mass (ATLAS$^{\rm 3D}$) and high-mass (MASSIVE) early-type systems.

4.2. *Linking the X-ray & optical properties of massive early-type galaxies*

Several origins for the hot gas surrounding early-type galaxies have been proposed in the previous decades, such as accretion from extremely large scales (Forman et al. 1985; Trinchieri & Fabbiano 1985) or from stellar mass loss material due to evolved stars (e.g., Mathews 1990; Brighenti & Mathews 1997; Mathews & Brighenti 2003). The simplest self-similar expectation for the X-ray luminosity of the gas is that $L_{\rm X,gas} \sim m_{\rm gas} T_{\rm gas}^2$. Assuming a galactic origin for the gas, one would then expect a significant correlation between $L_{\rm X,gas}$ and the galaxy stellar mass and/or the stellar velocity dispersion. X-ray observations have demonstrated that early-type galaxies with similar stellar masses can have vastly different X-ray properties (Forman et al. 1985; O'Sullivan et al. 2001; Mathews & Brighenti 2003; Bogdán & Gilfanov 2011), resulting in significant scatter in these relations. In the following sections, we combine the X-ray and optical properties of our sample of early-type galaxies. Using the large baselines in stellar mass, velocity dispersion, environment, galaxy rotation and accretion rates afforded by our sample, we can explore the parameters that may drive the scatter previously seen in the X-ray–optical relations.

[6] Due to our adopted parameterization of the X-ray spectra, the resultant best-fit temperature measurement within R_e for sources with low-$L_{\rm X,gas}$ ($< 10^{39}\,{\rm erg\,s^{-1}}$; low number of source counts) is degenerate around $T \sim 0.3-0.4$ keV, due to roughly equivalent contributions of the ISM, unresolved LMXBs and/or AB/CV components in the X-ray spectroscopy. Due to this degeneracy, sources with ISM at $T \lesssim 0.3$ keV are biased marginally high, and the measured uncertainties on $T_{\rm gas}$ are large (>50%), as shown in Fig 6a. Hence, we measure a marginally steeper slope of $\sim$4.7 for the full (ATLAS$^{\rm 3D}$ + MASSIVE) sample, though this is within the 1-σ uncertainty of that found by Kim & Fabbiano (2015) and when only considering the more robust measurements of the MASSIVE galaxies.

[7] NGC 1129 is a distinct outlier from the observed $L_{\rm X,gas}$–$T_{\rm gas}^{4.5}$ relation. NGC 1129 is the central galaxy of the poor group AWM7. There are two clear X-ray peaks within AWM7, one centered on the 2MASS position of NGC 1129, and the other offset ~ 1 kpc eastwards (Furusho et al. 2003). The X-ray surface brightness (SB) profile is strongly peaked, with small scale disturbances in the core, with evidence for bulk motions and a cooling flow (Neumann & Boehringer 1995; Furusho et al. 2003). Additionally, there are small SB depressions indicative of gas density fluctuations (Sanders & Fabian 2012). Given the short cooling time of the group ($\sim$ 0.4 Gyr; Cavagnolo et al. 2009) as well as evidence for a recent merger given the radial twist in the galaxy morphology (Peletier et al. 1990), it is likely that the gas within $1R_e$ will relax and rapidly cool to a gas temperature more consistent with the velocity-dispersion of NGC 1129 (see section 4.3).

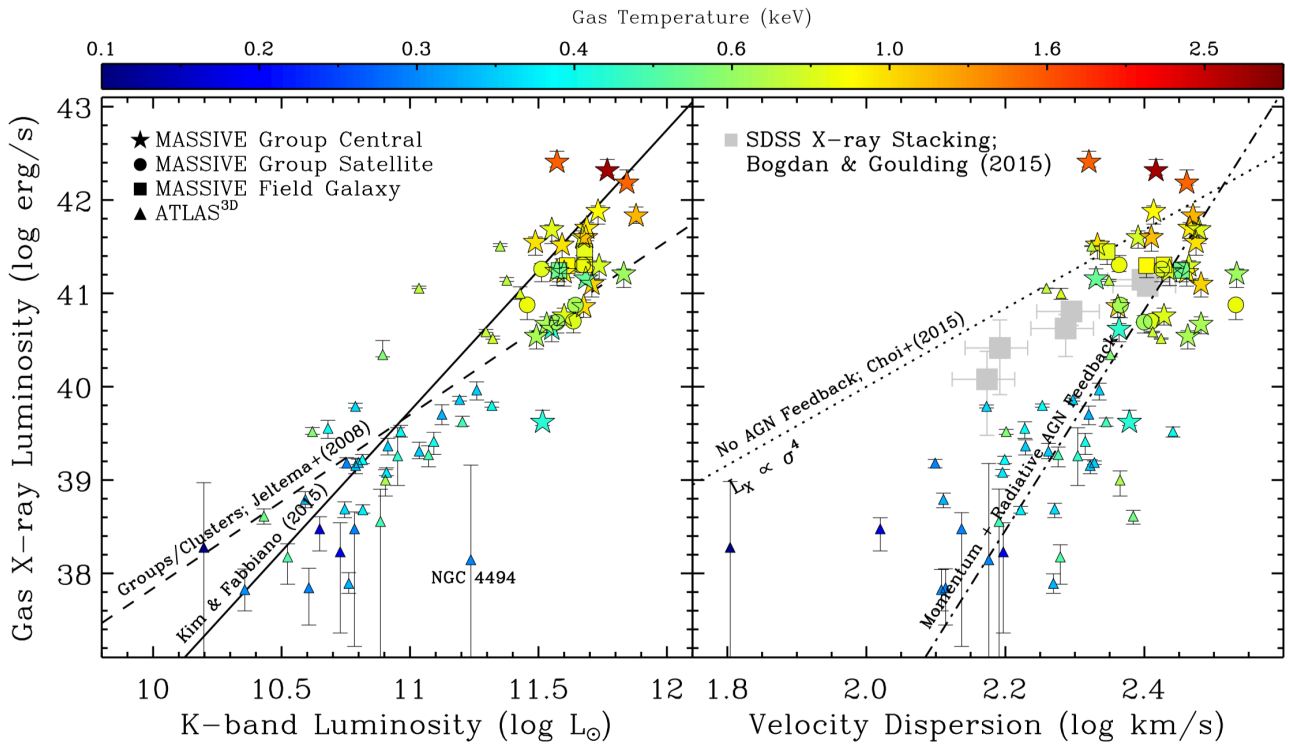

FIG. 7.— **Left:** Logarithm of 0.3–5.0 keV X-ray luminosity (in units of erg/s) of the diffuse gas measured within optical radii of the galaxy versus K-band luminosity (in units of solar luminosities). Stars represent the MASSIVE galaxies considered to be at the centers of their respective group halos (Crook et al. 2007). Circles represent MASSIVE galaxies considered to be satellite galaxies within the group halo. Squares represent the field galaxies. ATLAS^{3D} galaxies are shown with filled triangles (see Section 2.5 and Appendix). The $L_{\rm X,gas}$–L_K relations for individual ellipticals (Kim & Fabbiano 2015) and groups/clusters (Jeltema et al. 2008) are shown as solid and dashed lines, respectively. Our best-fit relation is $L_{\rm X,gas} \propto L_K^{2.5-2.8}$ with intrinsic scatter $\epsilon_{int} \sim 0.44-0.74$ dex. **Right:** Logarithm of 0.3–5.0 keV X-ray gas luminosity (in units of erg/s) versus the stellar velocity dispersion measured out to one effective radius (in units of km/s). Large filled gray square symbols show the $L_{\rm X,gas}$ measurements found from X-ray stacking of SDSS elliptical galaxies (Bogdán & Goulding 2015). Cosmological hydrodynamical simulations of the predicted X-ray luminosity arising during the formation of galaxies when the effects of mechanical and radiation driven feedback (dash-dot line) and no AGN feedback (dotted line; i.e., a self-similar $L_{\rm X,gas} \propto \sigma_e^4$ relation) are included (Choi et al. 2015). Our best-fit relation is $L_{\rm X,gas} \propto \sigma_e^{6.5-8.7}$ with intrinsic scatter $\epsilon_{int} \sim 0.71-0.97$ dex. **Common:** Color scaling represents the gas X-ray temperature derived from the X-ray spectral fitting analyses (see Section 3.2 and Appendix).

4.2.1. *The $L_{\rm X,gas}$–L_K relation*

Many previous investigations have sought to identify the relationship between the X-ray luminosity of the hot gas and the galaxy stellar content, most succinctly probed in the near-IR. In Figure 7, we show the relation between the total K-band luminosity (L_K), taken directly from the 2MASS extended source catalog (parameter `k_m_ext`), and X-ray luminosity of the hot gas component ($L_{\rm X,gas}$) extracted within a $1R_e$ aperture[8].

Although the MASSIVE galaxy sample spans a relatively modest range in L_K ($\sim (3-8)\times10^{11}$ L$_\odot$) the range covered in $L_{\rm X,gas}$ is many times larger. Even considering only the hot gas entrained within $1R_e$, the range in $L_{\rm X,gas}$ for these systems is, on average, almost ~ 2 orders of magnitude at a given L_K, which increases to $\sim$3 orders of magnitude if we include the low-luminosity outlier, NGC 5322.

To provide the largest baseline in stellar mass, in Fig. 7a we additionally include the X-ray and K-band luminosities for the ATLAS^{3D} early-type galaxies (see Section 2.5 and the Appendix). Similar to Section 4.1, we perform a linear regression using LINMIX_ERR (Kelly 2007) to include the uncertainties in both L_X and L_K (for the combined ATLAS^{3D} and MASSIVE galaxies). We find that the best fit relation goes as $L_{\rm X,gas} \propto L_K^{2.5-2.8}$ (for 67% of the posterior samples). The intrinsic scatter is determined to be $\sim 0.44-0.74$ dex for the posterior draws, but characterized by an asymmetric distribution with a significant tail out to $\sim$1.1 dex.[9] We find no clear evidence for a break in the $L_{\rm X,gas}-L_K$ relationship as both galaxy samples, when fit independently, are characterized by similar slopes ($\propto L_K^{\approx 2.7}$) and both present similar scatter (median ≈ 0.6 dex). Hence, the MASSIVE galaxies provide a smooth continuation of the $L_{\rm X,gas}-L_K$ relationship determined for the ATLAS^{3D}. Our observed slope for MASSIVE+ATLAS^{3D} measured within R_e is marginally flatter than the slope (3 ± 0.4) presented in Kim & Fabbiano (2015) based solely on large aperture measurements of the ATLAS^{3D} galaxies.

[8] As we provide clear evidence to in Figure 6, the X-ray properties of even the most massive elliptical galaxies (irrespective of their larger-scale environments) when measured at $r < R_e$ are consistent with the same scaling as early-type field galaxies. Given our goal is to probe the link between the optical and X-ray properties, we will consider only the X-ray measurements from the R_e aperture for all subsequent analyses.

[9] We note that the choice of a 3-Gaussian mixture model versus a flat prior does not result in significant differences in the slope or the derived intrinsic scatter of the fitted relation.

We find that the shallower $L_{\rm X,gas} - L_K$ relationship described by the groups and cluster systems ($L_{\rm X,gas} \propto L_K^{1.9}$) outlined in Jeltema et al. (2008; see also Mulchaey & Jeltema 2010) provides a lower envelope that almost a third of the MASSIVE sample lie on or close to. Our limited sample size does not allow us to probe for a divergence into two branches of the $L_{\rm X,gas} - L_K$ relationship at $L_K \gtrsim 2\times10^{11}$ L$_\odot$. At a given L_K, there appears to be little or no difference between the measured $L_{\rm X,gas}$ of isolated/field early-type galaxies and those residing close to the center of a group (central galaxies), suggesting that large-scale environment does not primarily drive the observed $L_{\rm X,gas}$ at a given L_K.

Overall, due to the smooth transition observed between the ATLAS$^{\rm 3D}$ and MASSIVE samples, across the full range in L_K considered here, we find little evidence that there is a particular L_K threshold where early-type galaxies become less effective at retaining their gas haloes.

4.2.2. *The $L_{\rm X,gas}$–σ_e relation*

Some recent studies argue that the stellar velocity dispersion, set by the galaxy's gravitational potential, may provide a better tracer of the hot gas. Assuming that the gas entrained in the gravitational potential is virialized, self-similarity predicts $L_{\rm X,gas} \propto \sigma^4$. This has previously been observed in galaxy clusters (e.g., Mushotzky & Scharf 1997; Mulchaey & Zabludoff 1998; Wu et al. 1999; Helsdon & Ponman 2000; Xue & Wu 2000; Mahdavi & Geller 2001; Ortiz-Gil et al. 2004). However, several relations between total $L_{\rm X,gas}$ and σ have been reported for elliptical galaxies, with exponents ranging from $\sim 8-14$ (including uncertainties; e.g., Eskridge et al. 1995; Mahdavi & Geller 2001; Diehl & Statler 2007).

In Figure 7b we show the $L_{\rm X,gas} - \sigma$ distribution for the MASSIVE and ATLAS$^{\rm 3D}$ galaxies. With the inclusion of the higher-mass early-type galaxy sample from MASSIVE, a correlation between $L_{\rm X,R_e}$ and σ_e clearly continues towards high values of $L_{\rm X,gas}$, following a steep $\sigma_e^{6.5-8.7}$ (for 67% of the posterior samples) relationship, and an intrinsic scatter of $\sim$0.71–0.97 dex.

In Figure 7b, we highlight the stacked X-ray luminosities and average velocity dispersion bins derived from SDSS galaxies in Bogdán & Goulding (2015). Though not fully inconsistent, given the large uncertainties of the stacked measurements, the $L_{\rm X,gas}$ derived from stacking are systematically high at $\sigma_e \sim 160$km/s when compared to the ATLAS$^{\rm 3D}$ sample. While statistically complete, the Bogdán & Goulding (2015) analysis performed with the ROSAT X-ray telescope lacked the angular resolution as well as sufficient signal-to-noise in the stacked X-ray images to probe ellipticals with low stellar mass or low stellar velocity dispersions. In the narrow luminosity range, $L_{\rm X,gas} \sim (0.9-3)\times10^{40}\,{\rm erg\,s^{-1}}$, where the SDSS stacking results are most complete, our individual detections are considerably lower than the $L_{\rm X,gas}$ observed in the X-ray stacks. This excess seen in the stack may be of physical origin due to contamination at large scales (due to the poor angular resolution of ROSAT) or may be induced by the presumption of a single gas temperature for each stack when calculating X-ray luminosities, as we show in Section 4.3, galaxies with low-σ_e have systematically lower gas temperatures. Alternately, there may be a long tail in the luminosity distribution towards high-$L_{\rm X,gas}$ at low- to moderate-σ_e that systematically drives up the mean $L_{\rm X,gas}$ observed in the stacks.

The steeper slope observed for the individual galaxies over that from the X-ray stacking results is similar to that predicted by recent hydrodynamical simulations (e.g., Choi et al. 2015). These models predict systematically lower X-ray luminosities than those expected from a self-similar ($\propto \sigma_e^4$) origin due to the injection of energy back into the thermal ISM or the removal of hot gas by mechanical and radiatively-driven AGN feedback. For a given σ_e these feedback models produce $L_{\rm X,gas}$ in line with the general trend we find in Figure 7b. However, we show that AGN may play less of a role for high-σ_e galaxies, as these sources do not diverge significantly from a more simple self-similar model that does not require feedback.

4.2.3. *The scatter in $L_{\rm X,gas}$–L_K versus $L_{\rm X,gas}$–σ_e*

The combination of the MASSIVE and ATLAS$^{\rm 3D}$ galaxies afford the opportunity to ascertain the fundamental relationship between the hot gas and the galaxy properties, as well as place constraints on the properties that may drive the scatter in these relations. We use a Bayesian bi-sector estimator to compare the dispersions between $L_{\rm X,gas}$, L_K and σ_e while correctly accounting for the uncertainties in the (in)dependent variables. From the previous sections, we find that the intrinsic scatter in these relationships goes as $\epsilon(L_{\rm X,gas}/\sigma_e) \sim 0.71-0.97$ dex and $\epsilon(L_{\rm X,gas}/L_K) \sim 0.44-0.74$ dex. To zeroth order, this could suggest that the hot gas and the galaxy are linked primarily through the stellar mass and not the gravitational potential (probed by σ_e). However, there are individual early-type galaxies, such as NGC 4342 and NGC 4291, that have values of $L_{\rm X,gas}$ that are 10–30 times larger than other galaxies with similar L_K (see Bogdán et al. 2012a,b), but have high values of σ_e that provides are far better prediction of $L_{\rm X,gas}$.

There are several observational and physical origins to the scatter in these relations. Measurement uncertainties in R_e and projection effects could both contribute to systematics in L_K, σ_e and $L_{\rm X,gas}$ on a galaxy-to-galaxy basis. However, these uncertainties are likely to be small compared to the observed scatter.

In Fig 7 we provide the associated gas temperatures of both the ATLAS$^{\rm 3D}$ and MASSIVE samples. At a given L_K or σ_e, we show in Figure 7 that the measured $L_{\rm X,gas}$ is strongly dependent on the gas temperature, and hence, the dominant source of scatter in these X-ray–optical relations may be due to gas temperature variations. To quantify the dependence of $L_{\rm X,gas}$ on $T_{\rm gas}$ at fixed L_K, we take the narrow range in $\log(L_K/L_\odot) \sim 11.25-11.75$ defined by our MASSIVE sample alone and refit the relation between $L_{\rm X,gas}$–$T_{\rm gas}$ for these objects. We determine that for a fixed value of L_K, $L_{\rm X,gas} \propto T_{\rm gas}^{4.1\pm0.4}$, which is consistent with our earlier finding of a univeral relationship between $L_{\rm X,gas}$ and $T_{\rm gas}$ in Section 4.1. By contrast, if we fix $L_{\rm X,gas}$, we find no such dependence on $T_{\rm gas}$ with L_K ($L_K \propto T_{\rm gas}^{-0.1\pm0.4}$) for those sources with $L_{\rm X,gas} \sim 10^{39} - 10^{40}\,{\rm erg\,s^{-1}}$. Furthermore, we determine that those early-type galaxies that lie below the $L_{\rm X,gas} - L_K$ relation of Kim & Fabbiano (2015), and hence have relatively low $L_{\rm X,gas}$ (i.e., they are possi-

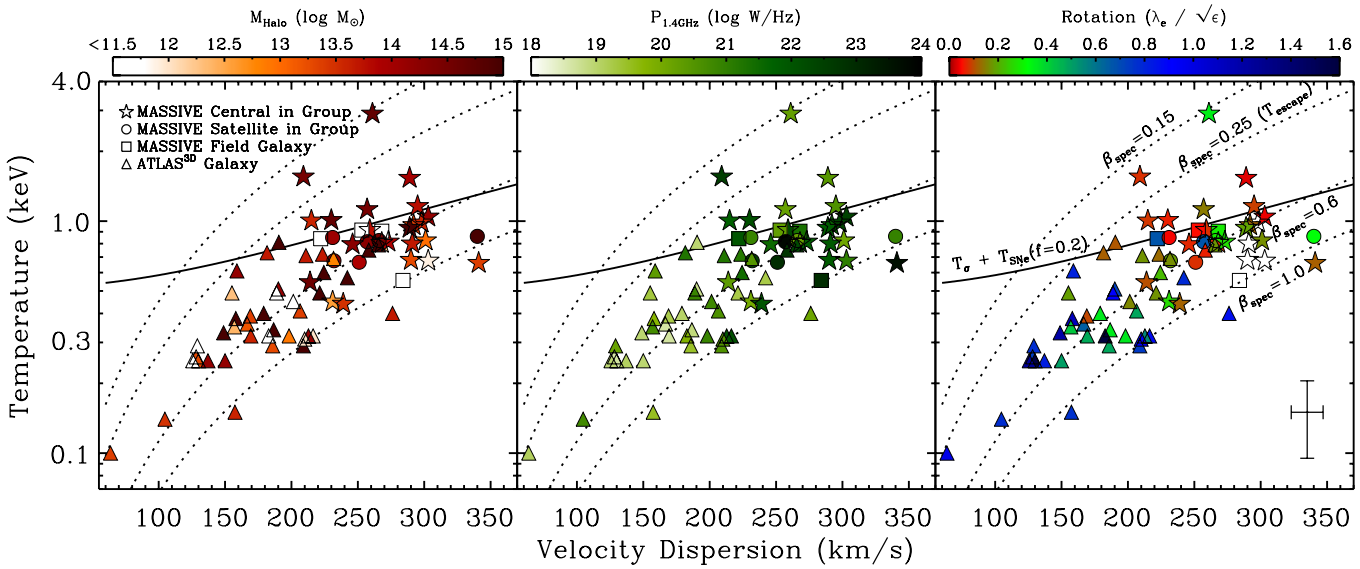

FIG. 8.— X-ray gas temperature (in units of keV) versus the stellar velocity dispersion (in units of km/s) measured within R_e. Symbols have the same meaning as previous figures. The best-fit $T-\sigma_e$ relation goes as $\sigma_e^{1.3-1.8}$ with an intrinsic scatter of $\sim 0.13-0.16$ dex. The idealized gas virial temperature, $\beta_{\rm spec} = \mu m_p \sigma_e^2 / kT_{\rm gas} = 1$, $\beta_{\rm spec} = 0.6$,0.25 and 0.15 are shown with dotted lines). The mass-averaged injection temperature produced due to perceived supernovae activity (i.e., the sum of the virial temperature and the gas temperature from SNe with $f = 0.2$; see Pellegrini (2011)) is shown with a solid line. Color gradient provides the total mass of the large (group-scale) halo (left panel; Crook et al. 2007); logarithm of the 1.4 GHz radio power in W/Hz (center panel); and galaxy rotation factor ($\lambda_e/\sqrt{\epsilon}$; right panel).

bly gas-poor for their stellar mass), typically exhibit the coolest gas temperatures ($T_{\rm gas} \sim 0.2$–0.4).

Given that the $L_{\rm X,gas}-L_K$ and $L_{\rm X,gas}-\sigma_e$ relations are strongly dependent on $T_{\rm gas}$, we suggest that when considered in isolation, neither L_K or σ_e alone are capable of accurately predicting $L_{\rm X,gas}$ for an early-type galaxy. Thus, care must be taken when using these scaling relations for objects lacking a constrained $T_{\rm gas}$ measurement. The gas temperature is likely to be driven by the gravitational potential well of the system (see Section 4.3) with secondary contributions from energy injection imparted by stochastic effects that may differ on a galaxy-to-galaxy basis, such as from a variety of internal and external processes such as gas/halo/stellar stripping, galaxy–galaxy mergers, and AGN feedback that imparts energy back into the thermal ISM and/or the dark matter halo. These differing heating/cooling/feedback effects likely influence the wide range in gas temperature for galaxies with similar L_K or σ_e, and hence, this results in the high scatter seen in Figure 7. In the next section, we use our optical data to further address how gas temperatures may drive this observed scatter.

4.3. $T_{\rm gas}-\sigma_e$: *probing the relationship between gas temperature and gravitational potential*

Both $L_{\rm X,gas}-L_K$ and $L_{\rm X,gas}-\sigma_e$ present large scatter and exhibit a clear dependence on gas temperature. Here we specifically investigate what drives the scatter in $T_{\rm gas}$ at a given σ_e, i.e., we ask whether $T_{\rm gas}$ is related to σ_e as expected from virial arguments. On the largest scales, studies have shown that the relationship between the intra-cluster gas temperature and the velocity dispersion of the galaxies is consistent with arising solely due to virial arguments (e.g., Wu et al. 1999; Xue & Wu 2000), while conflicting results have been found on whether the virial theorem holds for systems with lower temperature ($T < 1$ keV; e.g., White & Sarazin 1991; Ponman et al. 1996; White et al. 1997; Mulchaey & Zabludoff 1998; Xue & Wu 2000; Pellegrini 2011 and references there-in).

Figure 8 presents the $T_{\rm gas}-\sigma_e$ distribution for the MASSIVE and ATLAS$^{\rm 3D}$ galaxy samples. A Pearson-test reveals a significant correlation (at the >99.99% level) between $T_{\rm gas}$ and σ_e, with $r = 0.78$ for a two-tail test with 72 degrees of freedom. By applying the same Bayesian estimator as before (see section 4.2), we find that $T_{\rm gas} \propto \sigma_e^{1.3-1.8}$, with intrinsic scatter of $\sim 0.13-0.16$ dex. This scaling is marginally flatter than the simple virial expectation of σ_e^2, and is similar to that found by Davis & White (1996) using ROSAT data. Using the same Bayesian bi-sector method as in the previous section, we compare the scatter in $T_{\rm gas}-\sigma_e$ to the $L_{\rm X,gas}-L_K$ and $L_{\rm X,gas}-\sigma_e$ relations, finding that the scatter in $T_{\rm gas}-\sigma_e$ is a factor ~ 2 and 4 smaller, respectively. Hence, the scatter observed in the $T_{\rm gas}-\sigma_e$ relation is significantly smaller than the scatter found in any relation containing $L_{\rm X,gas}$. This in turn suggests that the gas temperature is fundamentally connected to the galaxy potential.

The galaxies considered here cover a significant range in both gas temperature ($T_{\rm gas} \sim 0.1-3.0$ keV) and velocity dispersion ($\sigma_e \sim 60$–330 km/s). In Figure 8 it is abundantly clear that there are no high velocity dispersion galaxies ($\sigma_e > 250\,{\rm km\,s^{-1}}$) with low gas temperatures ($T < 0.5$ keV). This apparent paucity of objects is expected assuming a virial origin for the heating of the gas. By comparing our sample to the simplest theoretical prediction for the virial gas temperature, such that $\beta_{\rm spec} = \mu m_p \sigma^2 / kT_{\rm gas}$, where m_p is the mass of a proton, μm_p is the mean particle mass with $\mu = 0.62$, and k is the Boltzmann constant (e.g., Loewenstein & White 1999; Loewenstein 2000; Sun et al. 2007; Jeltema et al. 2008; Pellegrini 2011), we show that within the

measurement uncertainties, no galaxies considered here have $\beta_{\rm spec} > 1$ suggesting that a virial model provides a lower-boundary to the observed gas temperature in early-type galaxies (e.g., Cox et al. 2006). Hence, we find good evidence that in all systems, the minimum gas temperature, $T_{\rm gas,min}$, goes as σ_e^2.

Consistent with previous results (e.g., Loewenstein & White 1999), the median $\beta_{\rm spec}$ for the sample is ~ 0.6. A median $\beta_{\rm spec} < 1$ suggests that, on average, every galaxy is under-going (or has recently undergone) some form of supplemental heating from internal/external processes (e.g., SNe feedback; star-formation; AGN feedback; large-scale environment; galaxy dynamics), such as those highlighted in some theoretical studies (e.g., Pellegrini 2011; Negri et al. 2015) or are undergoing a rapid cooling phase back to the virial temperature. Such a finding is also consistent with detailed studies of radial entropy profiles in some nearby systems, finding excess entropy over that expected from gravitational heating alone (e.g., Humphrey et al. 2008, 2011, 2012; Werner et al. 2012). This excess heating must occur on time scales shorter than the cooling time of recently acquired gas (e.g., for NGC 1129 $t_{\rm cooling} < 0.4$ Gyr). A median $\beta_{\rm spec} < 1$ may also hint at the dark matter halo playing a significant role in heating the gas above the virial temperature (e.g., Davis & White 1996; Loewenstein & White 1999). However, in this study we measured $T_{\rm gas}$ on R_e scales, and at these radii the stellar mass dominates the gravitational potential (e.g., Humphrey et al. 2006, 2009). As such, the effect of heating due to the halo should still be small. In Figure 8, we further utilize available ancillary data to probe the scatter in $\beta_{\rm spec}$ for our galaxy sample to place constraints on the heating mechanisms.

4.3.1. *The role of large-scale environment in X-ray gas heating*

A galaxy property that has been readily investigated in the literature is that of the large-scale environment. There is an expectation that the large scatter in the X-ray temperature or luminosity at a given stellar mass is, in part, due to the large scale environment of the galaxy, i.e., group/cluster-scale effects. Galaxies embedded at the center of a group should retain their hot gas, and are predicted to have enhanced X-ray emission due to the group gas. By contrast, satellite systems are expected to lose gas due to ram-pressure or viscous stripping. Recent studies have focused on small samples of isolated early-type galaxies in order to mitigate the effects of the host entrained as part of the intra-cluster medium. However, results have been inconclusive, with these investigations determining that some isolated systems retain their hot ISM, while others do not (e.g., Bogdan et al. 2012; Kim & Fabbiano 2013).

In the left panel of Figure 8 we include an estimate of the total halo mass measured from the motions of galaxies in the group taken from the 2MRS (Crook et al. 2007). The nine most isolated galaxies (i.e., those in the smallest halos) considered here span relatively wide ranges in temperature ($T \sim 0.2-0.9$ keV) and velocity dispersion ($\sigma_e \sim 120-290\,{\rm km\,s^{-1}}$). If the environment plays a substantial role in the central gas temperature, then isolated galaxies should have lower temperature and lower scatter. We find no evidence for such an environment-driven scenario in this sample; the parameter space occupied by isolated galaxies at fixed σ_e is the same as that for galaxies that reside in the most massive environments.

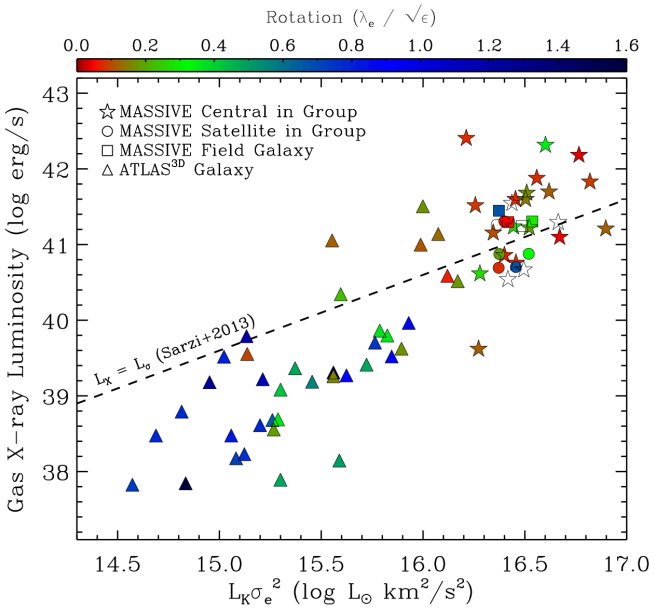

FIG. 9.— Logarithm of 0.3–5.0 keV X-ray luminosity of the diffuse halo gas versus K-band luminosity multiplied by the square of the central stellar velocity dispersion (i.e., the kinetic energy associated with stellar motion). Symbols have the same meaning as previous figures. Color gradient represents the 2-D rotational parameter $\lambda_R \sim \langle R|V|\rangle/\langle R\sqrt{V^2+\sigma_*^2}$, measurements are taken from Veale et al. (in prep.) and Emsellem et al. (2011). The nominal separation between fast and slow rotators is $\lambda_{R_e} = 0.31\sqrt{\epsilon}$. Following Sarzi et al. (2013), we show the theoretical prediction for the X-ray gas being produced due to stellar mass loss material ($L_{\rm X,gas} = L_\sigma = \frac{3}{2}\dot{M}\sigma_e^2$), dashed-line.

4.3.2. *The role of outflows in X-ray gas heating*

A further source of heating could be due to energy imparted due to out-flowing material, conceivably in the form of a radio jet due to black hole accretion or a supernova driven wind. Radio inflation of X-ray cavities shock heats and redistributes gas to large radii (see Finoguenov & Jones 2002; Forman et al. 2005; McNamara & Nulsen 2007; Kraft et al. 2012; Bogdán et al. 2014). This gas remains trapped within the wider halo, but then rains back towards the galaxy and the incident ISM, giving rise to additional shocks as well as being subject to gravitational heating, causing the gas to be heated to higher temperatures (see Allen et al. 2006; Dunn et al. 2010). Here we investigate whether the increased gas temperatures seen in some of the sample may be due to mechanical heating in the form of an AGN-driven radio jet.

In Fig. 8b, we show the rest-frame NRAO VLA Sky Survey (NVSS) or Faint Images of the Radio Sky at Twenty-cm (FIRST) radio luminosities at 1.4 GHz ($P_{\rm 1.4GHz}$) for the ATLAS$^{\rm 3D}$ and MASSIVE galaxies measured using the integrated flux measurements provided in the appropriate radio catalog (see Table 1). We find a general trend of increasing radio luminosity with increasing σ_e. Such a trend is expected given the well-known relations between the radio-power and the mass of the stellar component and the central black holes (e.g., Best

et al. 2005), both of which σ is used as a proxy for. However, we find no obvious trend between $\beta_{\rm spec}$ and $P_{1.4\rm GHz}$, suggesting that radio power alone cannot be driving the scatter in the gas temperatures and/or that mechanical heating, specifically on the scale of the galaxy, has a limited effect. We note that of the two sources that exhibit temperatures in excess of that required for the gas to escape the system (i.e., $\beta_{\rm spec} < 0.25$), one galaxy (NGC 708) is among the most radio-luminous considered here with $P_{1.4\rm GHz} \sim 4 \times 10^{22}$ W/Hz. In NGC 708 the mechanical heating from the jet may be sufficient to expel the hot gas from the galaxy entirely. Indeed, in-depth studies of the cluster host, Abell 262, show a complex structure and cooling flow towards the central region surrounding NGC 708 with X-ray cavities inflated by radio lobes, suggesting a once powerful outflow (see Blanton et al. 2004). In line with these results, we find that the X-ray emitting gas within R_e is better fit by two separate temperature components with $T_1 \sim 2.0$ keV and $T_2 \sim 1.1$ keV. The cooler component has a substantially lower luminosity by a factor $\sim 5-7$ compared with the hot component. The more luminous component has a similar gas temperature to that found at larger radii, which may be the result of a recent merger between two large halos. However, we note the presence of a secondary bright galaxy that lies at a distance of $r < R_e$, which may also be the source of the cooler gas component.

Energy injection by supernovae (SNe) activity may induce shocks within the incident gas, and hence, may also play a role in heating. Of the ATLAS$^{\rm 3D}$ and MASSIVE galaxies with X-ray observations that have detectable hot gas emission, all have star-formation rates (SFRs) less than $\sim 0.1 M_{\odot}/{\rm yr}^{-1}$. Indeed, we show that at low-σ_e ($< 200\,{\rm km\,s^{-1}}$), where SNe may play a more impactful role in gas heating, all of the sources considered here fall significantly below the prediction for SNe heating of Pellegrini (2011) with $f = 0.2$, where f is the fraction of energy imparted by Type-1a supernovae that is converted to heat.

4.3.3. *The role of galaxy rotation in X-ray gas heating*

Intrinsic flattening and/or the rotation of a galaxy is believed to serve a role in the ability of a system to retain its hot gas (e.g., Eskridge et al. 1995; Ciotti & Pellegrini 1996; Brighenti & Mathews 1997). Using the apparent ellipticity (ϵ) in conjunction with the measurement of the system rotational support (λ_e), we parameterize the relative rotational speed of the galaxies, and separate our sample into slow and fast rotators (see Sections 2.3 and 2.5). We follow Sarzi et al. (2013) and in Figure 8c we confirm that the fastest rotators with $\lambda_e/\sqrt{\epsilon} \gtrsim 1.0$ are generally low σ_e galaxies with $\sigma_e \lesssim 150$ km/s, while the slowest rotators with $\lambda_e/\sqrt{\epsilon} \lesssim 0.2$ are the most massive systems with $\sigma_e \gtrsim 200$ km/s (see also Emsellem et al. 2011). Overall, there appears to be a smooth continuum with decreasing rotation for increasing $T_{\rm gas}$. Of the two galaxies with $\beta_{\rm spec} < 0.25$, NGC 708 is a slow rotator that may have its high gas temperature driven by a radio jet (see previous sub-section), while NGC 1129 is considered a fast rotator. Although these are only two objects, they may suggest that the temperature of the hot gas is primarily set by the galaxy central potential, but that a combination of other physical galaxy properties play a secondary role (e.g., galaxy rotation; mechanical heating from radio jets).

To probe this further, Sun et al. (2007) and Sarzi et al. (2013) present the $L_{\rm X,gas}$–$L_K\sigma_e^2$ diagram, which in-effect traces the X-ray luminosity expected due to the thermalization of the energy from stellar mass loss material. In this paradigm, L_K provides a tracer for the mass of the stars where the gas may originate, and σ_e^2 provides a proxy for the gravitational heating energy. This is in analog to the $L_B\sigma_e^2$ parameter introduced by Canizares et al. (1987). Based on the ATLAS$^{\rm 3D}$ sample alone, Sarzi et al. conclude that slow rotating early-type galaxies exhibit X-ray luminosities[10] that are sustained by the thermalization of stellar mass loss material, such that $L_X = L_\sigma = \frac{3}{2}\dot{M}\sigma_e^2$, while fast rotators lie significantly below this threshold. However, and as noted previously, the ATLAS$^{\rm 3D}$ sample contains few slow-rotators. To predict L_σ, their model assumes a stellar-mass-loss rate ($\dot{M}$) set by an extrapolation of L_K and the average stellar age of the population (see Ciotti et al. 1991; Sarzi et al. 2013 for further details).

In Figure 9, with the inclusion of a large number of slow rotators from the MASSIVE sample, we clearly show that (a) a simplistic stellar-mass loss model $L_{\rm X,gas} = L_\sigma$ does not provide a good description of the data, and (b) that deviations from this theoretical prediction are not correlated with the rotation properties of the galaxies. Fast and slow rotators are clearly present both above and below the $L_{\rm X,gas}$ prediction from stellar mass loss material. Further examining the dispersion along the $L_X = L_\sigma$ axis, we find a strong trend with gas temperature. The sources that lie significantly below the $L_X = L_\sigma$ prediction comprise the coolest early-type galaxies, while those that lie above the prediction possess the hottest gas temperatures.[11]

Although we find an apparent deviation from the theoretical prediction, we cannot yet rule out that stellar mass loss dominates the gas supply in these galaxies. Substantial uncertainty remains in the mass loss rates. Taking empirical scalings based on individual AGB stars yields ∼50% level differences in the expected mass-loss rates (Athey et al. 2002). However, the impact of stellar age and metallicity on the mass-loss rates, while important, have not been adequately calibrated. In particular, both stellar age and metallicity provide additional parameters in this scaling. The zeroth order relation shown here assumes a constant age, but Ciotti et al. (1991) suggest that $\dot{M}$ scales as $t_{\rm age}^{-1.3}$. In fact, including the steadily increasing age towards more massive galaxies would make the discrepancy between model and data worse. The other possible second parameter is metallicity. More massive early-type galaxies are also more metal rich (e.g., Trager et al. 2000; McDermid et al. 2014; Greene et al. 2015), which naturally leads to more mass loss per unit mass. Thus, one possible explanation for

[10] In the Sarzi et al. (2013) study, the X-ray measurements are taken from Boroson et al. (2011).

[11] We note that if we compare the MASSIVE sample to the ATLAS$^{\rm 3D}$ sample using the Boroson et al. (2011) X-ray measurements our conclusions remain qualitatively consistent. Our conclusions are mainly driven by the increased dynamic range in stellar mass afforded by our combined (MASSIVE+ATLAS$^{\rm 3D}$) galaxy sample.

the mismatch between the expected luminosity due to mass loss and that observed, simply arises due to our presumed model of mass loss. A third possibility is that the low-mass galaxies are simply less effective at retaining their gas (e.g., due to more recent star formation episode, ram-pressure stripping), while the discrepancies at the high-mass end are caused by innacuracies in the mass-loss models. The flattening of galaxies, particularly in slow rotators, may also play a role here. While beyond the scope of this work, it will be very interesting in the future to see if more realistic models of mass loss can explain the full range of observed X-ray luminosities.

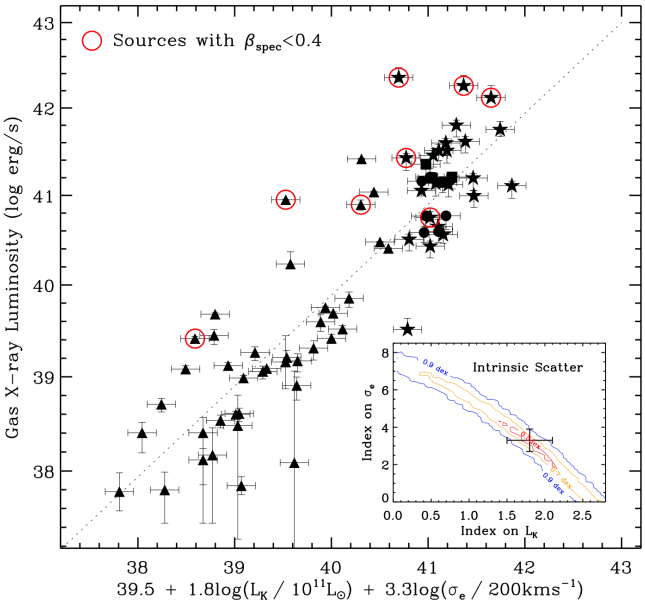

FIG. 10.— Logarithm of 0.3–5.0 keV X-ray luminosity of the diffuse halo gas versus the multivariate relationship for L_K and σ_e described in Section 4.4 for all ellipticals in the MASSIVE and ATLAS^{3D} samples. Dotted line represents the 1:1 relation between the empirical relation and $L_{X,gas}$. Filled symbols have the same meaning as previous figures. Red open circles represent outliers in the $T_{gas} - \sigma_e$ relation with $\beta_{spec} < 0.4$. Inset figure shows the best fit and associated uncertainties to the indices in the derived $L_K^\alpha \sigma_e^\gamma$ empirical relation. Contours represent the median intrinsic scatter of the posterior draws in the derived relations as a function of the indices α and γ (contours levels – red:0.5 dex; yellow:0.7 dex; blue:0.9 dex).

4.4. *An empirical two-optical-parameter X-ray–optical relation*

$L_K\sigma_e^2$ provides a simple model for the origin of $L_{X,gas}$, harnessing L_K and σ_e as proxies for the stellar-mass content and the gravitational heating, respectively. However, as we show in the previous section, this particular parameterization is clearly a poor description of the data. Here we attempt to improve on this scaling relation, following an empirical approach based on our large galaxy sample. Following Sun et al. (2007) and Sarzi et al. (2013), we attempt to parameterize $L_{X,gas}$ using the same optical proxies, but now introducing free variables for the index powers, such that $L_{X,gas} \sim L_K^\alpha \sigma_e^\gamma$.

We perform a Bayesian multi-variate linear regression analysis in logarithmic space that seeks to find the best-fit linear relation between $\log(L_K\sigma_e)$ and $\log(L_{X,gas})$. This process harnesses a modified version of the `LINMIX_ERR` algorithm (see Section 4.2) to sample the multi-dimensional parameter space while accounting for uncertainties in all three measured parameters in order to minimize the intrinsic scatter between the observables. The fitting process maintains flat residuals between $L_{X,gas}$ and the fit to $L_K^\alpha \sigma_e^\gamma$ (i.e., forcing a 1:1 relation between $L_{X,gas}$ and $L_K^\alpha \sigma_e^\gamma$). This stipulation of flat residuals forces the most conservative estimate of the intrinsic scatter between the variables during the fit.

We find that the best-fit empirical relation goes as $L_{X,gas} = a\log(L_K/10^{11}\,L_\odot) + b\log(\sigma_e/\mathrm{km/s}) + c$, where $a = 1.8 \pm 0.3$, $b = 3.3 \pm 0.6$ and $c = 39.5 \pm 0.4$ (see Figure 10) with an intrinsic scatter of ~ 0.41–0.47 dex. The steep dependence on L_K (an exponent ~ 2) that is preferred during the fitting process likely arises due to the wide range in T_{gas} at a given L_K that was observed in Figure 7a, compounded with the steep slope of the $L_{X,gas} - T_{gas}$ relation found in Section 4.1. However, we also note that we still may not be probing the full range in gas temperatures that may exist in the entire galaxy population at a given L_K, particularly at low stellar masses, due to selection biases related to the sources chosen for X-ray observations.

Finally, in Figure 10, we highlight the eight sources that are $\gtrsim 2\sigma$ outliers from the best-fit $\beta_{spec} \sim 0.6$ relation (i.e., those sources with high T_{gas} based on a virial origin for the gas heating). We find that the majority are systematically shifted towards higher values of $L_{X,gas}$ based on the $L_{X,gas}$ predicted from our empirical fit to the optical properties. This may suggest an additional form of heating or an increased gas mass that is not directly linked to the host galaxy. Hence, the large scatter found in the $L_{X,gas}$ relations may arise due to variations in m_{gas} (or M_{halo}) at fixed stellar mass. Such systems may exhibit significant cooling flows, particularly those that have experienced recent mergers. Future studies aiming to examine these changes in m_{gas} should endeavor to provide a complete and unbiased X-ray view of the full galaxy population for a given optical property.

5. SUMMARY

We have investigated the connection between the X-ray and optical properties of massive early-type galaxies in the nearby Universe. Using sensitive *Chandra* ACIS X-ray spectroscopy, we have measured the X-ray luminosity at 0.3–5 keV and temperatures of the hot gas entrained within the gravitational potential of the 33 sources selected from the volume-limited sample of 116 galaxies in the MASSIVE Survey that have suitable *Chandra* data. These 33 galaxies are among the most massive galaxies in the Universe with $L_K \gtrsim 3\times10^{11}\,L_\odot$ and within 108 Mpc. We combined our MASSIVE sample with 41 lower mass elliptical galaxies that have comparable optical integral field unit and X-ray measurements in the ATLAS^{3D} sample to investigate the X-ray–optical properties over the largest dynamic range in L_K.

We summarize our conclusions as follows:

1. We demonstrate that all early-type galaxies follow a universal scaling relation going as $L_{X,gas} \propto T_{gas}^{\sim 4.5}$, when the X-ray properties are measured within an optical effective radius of the galaxy. The observed scatter of ~ 0.5 dex about this relation is consis-

tent across the full considered parameter space. In addition, we further find the scatter is independent of secondary galaxy properties such as the galaxy rotational support or AGN activity ($P_{1.4\mathrm{GHz}}$). By careful comparison of the X-ray luminosities measured within optical radii and out to large radii, we conclude that excess X-ray luminosity observed in large aperture measurements of some massive ellipticals that lie within groups or clusters is likely the result of contamination from the large scale environment.

2. In accordance with prior studies, we show that the most massive early-type systems exhibit high X-ray luminosities that lie in the region of $L_{\mathrm{X,gas}} - L_K$ parameter-space roughly predicted by an extrapolation of the previously measured relationship, going as $L_{\mathrm{X,gas}} \propto L_K^{2.5-2.8}$. We demonstrate that the scatter about the $L_{\mathrm{X,gas}} - L_K$ relation is mostly driven by the X-ray temperature of the hot gas, with the hottest systems lying at higher $L_{\mathrm{X,gas}}$ compared to the simple $L_{\mathrm{X,gas}} - L_K$ prediction. We further show that similar qualitative inferences can be made for the galaxies when considered in $L_{\mathrm{X,gas}} - \sigma_e$ space. Given the significant scatter in both $L_{\mathrm{X,gas}} - L_K$ and $L_{\mathrm{X,gas}} - \sigma_e$, combined with an obvious temperature dependence, we draw no definitive conclusions about whether either of these relations (in isolation) can be considered intrinsic to early-type galaxies.

3. We find a statistically significant correlation between the stellar velocity dispersion and the X-ray gas temperature at the 99.99% level such that $T \sim \sigma_e^{1.6}$. The minimum observed X-ray temperature is consistent with being set directly by the gravitational potential of the system, with $\beta_{\mathrm{spec}} = \mu m_p \sigma_e^2 / kT_{\mathrm{gas}} = 1$. On average, we find that all galaxies experience some form of heating above the virial temperature, measuring a median $\beta_{\mathrm{spec}} \sim 0.6$. However, for those sources with X-ray temperatures significantly exceeding those expected from virial heating alone, we find no obvious links with the large scale environment of the galaxy (i.e., mass of the large scale halo), the presence of a radio jet, or the rotation/flattening of the galaxy.

4. We probe the importance of recycled gas in explaining the X-ray luminosity observed in early-type galaxies. We find that the simplest model, such that the X-ray luminosity is produced due to thermalization of the energy from stellar mass loss material, fails to reproduce the observations when a significant number of slow-rotating galaxies are included. Even when including the large uncertainties involved with deriving the mass-loss rates, other physical mechanisms are still required to explain the data in hand (e.g., a lack of gas retention at low mass; stochastic accretion at high mass).

5. We investigate the existence of an empirical relationship between $L_{\mathrm{X,gas}}$, L_K and σ_e. We calculate that the best fit multivariate relation is described as $L_{\mathrm{X,gas}} = a\log(L_K/10^{11}\,\mathrm{L}_\odot) + b\log(\sigma_e/\mathrm{km/s}) + c$, where $a = 1.8 \pm 0.3$, $b = 3.3 \pm 0.6$ and $c = 39.5 \pm 0.4$ with an intrinsic scatter of only ~ 0.41–0.47 dex. Those galaxies with $\beta_{\mathrm{spec}} < 0.4$ (i.e., with increased T_{gas} compared to the expected T_{virial}) have systematically high-$L_{\mathrm{X,gas}}$ than that expected from the best-fit relation possibly due to the presence of cooling flows or an increased gas mass in these systems.

We would like to thank the anonymous referee for useful and insightful comments that allowed us to strengthen our results and conclusions. We are thankful to Bill Forman, Christine Jones, Yuanyuan Su and Ming Sun for helpful discussions. ADG acknowledges funding from NASA grant AR3-14016X. Also JEG acknowledges support from the Miller Institute at Berkeley. This survey is supported in part by NSF AST-1411945 and AST-1411642. *Facilities:* Chandra (ACIS).

REFERENCES

Allen, S. W., Dunn, R. J. H., Fabian, A. C., Taylor, G. B., & Reynolds, C. S. 2006, MNRAS, 372, 21
Athey, A., Bregman, J., Bregman, J., Temi, P., & Sauvage, M. 2002, ApJ, 571, 272
Bell, E. F., et al. 2004, ApJ, 608, 752
Bender, R., Surma, P., Doebereiner, S., Moellenhoff, C., & Madejsky, R. 1989, A&A, 217, 35
Best, P. N., Kauffmann, G., Heckman, T. M., Brinchmann, J., Charlot, S., Ivezić, Ž., & White, S. D. M. 2005, MNRAS, 362, 25
Binney, J. 2005, MNRAS, 363, 937
Blakeslee, J. P., et al. 2003, ApJ, 596, L143
Blanton, E. L., Sarazin, C. L., McNamara, B. R., & Clarke, T. E. 2004, ApJ, 612, 817
Blanton, M. R., & Moustakas, J. 2009, ARA&A, 47, 159
Bogdán, Á., David, L. P., Jones, C., Forman, W. R., & Kraft, R. P. 2012a, ApJ, 758, 65
Bogdán, Á., & Gilfanov, M. 2008, MNRAS, 388, 56
—. 2011, MNRAS, 418, 1901
Bogdán, Á., & Goulding, A. D. 2015, ApJ, 800, 124
Bogdán, Á., et al. 2012b, ApJ, 753, 140
—. 2014, ApJ, 782, L19
Boroson, B., Kim, D.-W., & Fabbiano, G. 2011, ApJ, 729, 12
Brighenti, F., & Mathews, W. G. 1997, ApJ, 486, L83
Brown, B. A., & Bregman, J. N. 2000, ApJ, 539, 592
Bundy, K., et al. 2010, ApJ, 719, 1969
Buote, D. A. 2000, MNRAS, 311, 176
Canizares, C. R., Fabbiano, G., & Trinchieri, G. 1987, ApJ, 312, 503
Cappellari, M., & Emsellem, E. 2004, PASP, 116, 138
Cappellari, M., et al. 2011, MNRAS, 413, 813
—. 2013, MNRAS, 432, 1709
Cavagnolo, K. W., Donahue, M., Voit, G. M., & Sun, M. 2009, ApJS, 182, 12
Choi, E., Ostriker, J. P., Naab, T., Oser, L., & Moster, B. P. 2015, MNRAS, 449, 4105
Ciotti, L., D'Ercole, A., Pellegrini, S., & Renzini, A. 1991, ApJ, 376, 380
Ciotti, L., & Pellegrini, S. 1996, MNRAS, 279, 240
Civano, F., Fabbiano, G., Pellegrini, S., Kim, D.-W., Paggi, A., Feder, R., & Elvis, M. 2014, ApJ, 790, 16
Cowie, L. L., & Barger, A. J. 2008, ApJ, 686, 72
Cox, T. J., Di Matteo, T., Hernquist, L., Hopkins, P. F., Robertson, B., & Springel, V. 2006, ApJ, 643, 692
Crook, A. C., Huchra, J. P., Martimbeau, N., Masters, K. L., Jarrett, T., & Macri, L. M. 2007, ApJ, 655, 790

Davis, D. S., & White, III, R. E. 1996, ApJ, 470, L35
Davis, T. A., Greene, J., Ma, C.-P., Pandya, V., Blakeslee, J. P., McConnell, N., & Thomas, J. 2016, MNRAS, 455, 214
Diehl, S., & Statler, T. S. 2007, ApJ, 668, 150
—. 2008, ApJ, 687, 986
Dunn, R. J. H., Allen, S. W., Taylor, G. B., Shurkin, K. F., Gentile, G., Fabian, A. C., & Reynolds, C. S. 2010, MNRAS, 404, 180
Edge, A. C., & Stewart, G. C. 1991, MNRAS, 252, 428
Emsellem, E. 2013, MNRAS, 433, 1862
Emsellem, E., et al. 2007, MNRAS, 379, 401
—. 2011, MNRAS, 414, 888
Eskridge, P. B., Fabbiano, G., & Kim, D.-W. 1995, ApJS, 97, 141
Ettori, S., Tozzi, P., Borgani, S., & Rosati, P. 2004, A&A, 417, 13
Fabbiano, G. 2006, ARA&A, 44, 323
Faber, S. M., et al. 1997, AJ, 114, 1771
—. 2007, ApJ, 665, 265
Falcón-Barroso, J., Sánchez-Blázquez, P., Vazdekis, A., Ricciardelli, E., Cardiel, N., Cenarro, A. J., Gorgas, J., & Peletier, R. F. 2011, A&A, 532, A95
Ferrarese, L., van den Bosch, F. C., Ford, H. C., Jaffe, W., & O'Connell, R. W. 1994, AJ, 108, 1598
Ferrarese, L., et al. 2006, ApJS, 164, 334
Finoguenov, A., & Jones, C. 2002, ApJ, 574, 754
Forman, W., Jones, C., & Tucker, W. 1985, ApJ, 293, 102
Forman, W., et al. 2005, ApJ, 635, 894
Furusho, T., Yamasaki, N. Y., & Ohashi, T. 2003, ApJ, 596, 181
Gilfanov, M. 2004, MNRAS, 349, 146
Goulding, A. D., et al. 2012, ApJS, 202, 6
Greene, J. E., Janish, R., Ma, C.-P., McConnell, N. J., Blakeslee, J. P., Thomas, J., & Murphy, J. D. 2015, ApJ, 807, 11
Greene, J. E., Murphy, J. D., Graves, G. J., Gunn, J. E., Raskutti, S., Comerford, J. M., & Gebhardt, K. 2013, ApJ, 776, 64
Helsdon, S. F., & Ponman, T. J. 2000, MNRAS, 315, 356
Helsdon, S. F., Ponman, T. J., O'Sullivan, E., & Forbes, D. A. 2001, MNRAS, 325, 693
Hill, G. J., et al. 2008, in Astronomical Society of the Pacific Conference Series, Vol. 399, Panoramic Views of Galaxy Formation and Evolution, ed. T. Kodama, T. Yamada, & K. Aoki, 115
Huchra, J. P., et al. 2012, ApJS, 199, 26
Humphrey, P. J., Buote, D. A., Brighenti, F., Gebhardt, K., & Mathews, W. G. 2008, ApJ, 683, 161
—. 2009, ApJ, 703, 1257
Humphrey, P. J., Buote, D. A., Canizares, C. R., Fabian, A. C., & Miller, J. M. 2011, ApJ, 729, 53
Humphrey, P. J., Buote, D. A., Gastaldello, F., Zappacosta, L., Bullock, J. S., Brighenti, F., & Mathews, W. G. 2006, ApJ, 646, 899
Humphrey, P. J., Buote, D. A., O'Sullivan, E., & Ponman, T. J. 2012, ApJ, 755, 166
Jarrett, T. H., Chester, T., Cutri, R., Schneider, S. E., & Huchra, J. P. 2003, AJ, 125, 525
Jeltema, T. E., Binder, B., & Mulchaey, J. S. 2008, ApJ, 679, 1162
Kelly, B. C. 2007, ApJ, 665, 1489
Khosroshahi, H. G., Ponman, T. J., & Jones, L. R. 2007, MNRAS, 377, 595
Kim, D.-W., & Fabbiano, G. 2013, ApJ, 776, 116
—. 2015, ApJ, 812, 127
Kormendy, J., & Bender, R. 1996, ApJ, 464, L119
—. 2012, ApJS, 198, 2
Kormendy, J., Fisher, D. B., Cornell, M. E., & Bender, R. 2009, ApJS, 182, 216
Kraft, R. P., et al. 2012, ApJ, 749, 19
Krajnović, D., et al. 2011, MNRAS, 414, 2923
—. 2013, MNRAS, 433, 2812
Lauer, T. R., et al. 1995, AJ, 110, 2622
—. 2007, ApJ, 662, 808
Lehmer, B. D., et al. 2007, ApJ, 657, 681
—. 2014, ApJ, 789, 52
Loewenstein, M. 2000, ApJ, 532, 17
Loewenstein, M., & White, III, R. E. 1999, ApJ, 518, 50
Ma, C.-P., Greene, J. E., McConnell, N., Janish, R., Blakeslee, J. P., Thomas, J., & Murphy, J. D. 2014, ApJ, 795, 158
Mahdavi, A., & Geller, M. J. 2001, ApJ, 554, L129
Markevitch, M. 1998, ApJ, 504, 27
Mathews, W. G. 1990, ApJ, 354, 468
Mathews, W. G., & Brighenti, F. 2003, ARA&A, 41, 191
Maughan, B. J., Giles, P. A., Randall, S. W., Jones, C., & Forman, W. R. 2012, MNRAS, 421, 1583
McDermid, R. M., et al. 2014, ApJ, 792, L37
McNamara, B. R., & Nulsen, P. E. J. 2007, ARA&A, 45, 117
Memola, E., Trinchieri, G., Wolter, A., Focardi, P., & Kelm, B. 2009, A&A, 497, 359
Mitchell, R. J., Dickens, R. J., Burnell, S. J. B., & Culhane, J. L. 1979, MNRAS, 189, 329
Mittal, R., Hicks, A., Reiprich, T. H., & Jaritz, V. 2011, A&A, 532, A133
Mulchaey, J. S. 2000, ARA&A, 38, 289
Mulchaey, J. S., & Jeltema, T. E. 2010, ApJ, 715, L1
Mulchaey, J. S., & Zabludoff, A. I. 1998, ApJ, 496, 73
Mushotzky, R. F. 1984, Physica Scripta Volume T, 7, 157
Mushotzky, R. F., & Scharf, C. A. 1997, ApJ, 482, L13
Negri, A., Pellegrini, S., & Ciotti, L. 2015, MNRAS, 451, 1212
Neumann, D. M., & Boehringer, H. 1995, A&A, 301, 865
Ortiz-Gil, A., Guzzo, L., Schuecker, P., Böhringer, H., & Collins, C. A. 2004, MNRAS, 348, 325
Osmond, J. P. F., & Ponman, T. J. 2004, MNRAS, 350, 1511
O'Sullivan, E., Forbes, D. A., & Ponman, T. J. 2001, MNRAS, 328, 461
O'Sullivan, E., Ponman, T. J., & Collins, R. S. 2003, MNRAS, 340, 1375
Paggi, A., Fabbiano, G., Civano, F., Pellegrini, S., Elvis, M., & Kim, D.-W. 2015, ArXiv e-prints
Paturel, G., Petit, C., Prugniel, P., Theureau, G., Rousseau, J., Brouty, M., Dubois, P., & Cambrésy, L. 2003, A&A, 412, 45
Peletier, R. F., Davies, R. L., Illingworth, G. D., Davis, L. E., & Cawson, M. 1990, AJ, 100, 1091
Pellegrini, S. 2011, ApJ, 738, 57
Ponman, T. J., Bourner, P. D. J., Ebeling, H., & Böhringer, H. 1996, MNRAS, 283, 690
Revnivtsev, M., Churazov, E., Sazonov, S., Forman, W., & Jones, C. 2007, A&A, 473, 783
Sánchez-Blázquez, P., et al. 2006, MNRAS, 371, 703
Sanders, J. S., & Fabian, A. C. 2012, MNRAS, 421, 726
Sarzi, M., et al. 2013, MNRAS, 432, 1845
Sérsic, J. L. 1963, Boletin de la Asociacion Argentina de Astronomia La Plata Argentina, 6, 41
Sivakoff, G. R., Sarazin, C. L., & Carlin, J. L. 2004, ApJ, 617, 262
Su, Y., Irwin, J. A., White, III, R. E., & Cooper, M. C. 2015, ApJ, 806, 156
Sun, M., Jones, C., Forman, W., Vikhlinin, A., Donahue, M., & Voit, M. 2007, ApJ, 657, 197
Sun, M., Voit, G. M., Donahue, M., Jones, C., Forman, W., & Vikhlinin, A. 2009, ApJ, 693, 1142
Thomas, D., Maraston, C., Bender, R., & Mendes de Oliveira, C. 2005, ApJ, 621, 673
Thomas, J., et al. 2011, MNRAS, 415, 545
Trager, S. C., Faber, S. M., Worthey, G., & González, J. J. 2000, AJ, 119, 1645
Trinchieri, G., & Fabbiano, G. 1985, ApJ, 296, 447
Vajgel, B., Jones, C., Lopes, P. A. A., Forman, W. R., Murray, S. S., Goulding, A., & Andrade-Santos, F. 2014, ApJ, 794, 88
van Dokkum, P. G., et al. 2008, ApJ, 677, L5
—. 2010, ApJ, 709, 1018
Werner, N., Allen, S. W., & Simionescu, A. 2012, MNRAS, 425, 2731
White, D. A., Jones, C., & Forman, W. 1997, MNRAS, 292, 419
White, III, R. E., & Sarazin, C. L. 1991, ApJ, 367, 476
Wu, X.-P., Xue, Y.-J., & Fang, L.-Z. 1999, ApJ, 524, 22
Xue, Y.-J., & Wu, X.-P. 2000, ApJ, 538, 65
York, D. G., et al. 2000, AJ, 120, 1579
Young, L. M., et al. 2011, MNRAS, 414, 940

APPENDIX

CHANDRA X-RAY MEASUREMENTS OF ATLAS^{3D} GALAXIES

To provide the most accurate and complete comparison to our X-ray measurements of the MASSIVE galaxies, we require a sample of lower-mass early-type galaxies that have comparable X-ray observations. As stated in Section 2.5 of the main article, the ATLAS^{3D} galaxy survey provides the most natural comparison to the MASSIVE galaxies. Recently, Kim & Fabbiano (2015) and presented (constrained) X-ray gas and luminosity measurements of (49) 61 of the early-type galaxies in ATLAS^{3D} that have observations with the *Chandra* X-ray telescope. As stated previously, these measurements were performed using large apertures, which encompassed all of the detected X-ray photons that were possibly associated with the galaxy. Given that some of these sources were in group/cluster environments, we also require small aperture measurements, performed on the scales of the galaxy-radius, to limit contamination from the large-scale environment. Su et al. (2015) present X-ray measurements for a sub-sample of 37 of the 49 objects in Kim & Fabbiano (2015). Here we present X-ray measurements performed within R_e for the remaining 12 objects, as well as a comparison between the X-ray measurements presented here and those in Kim & Fabbiano (2015) and Su et al. (2015).

The *Chandra* data were retrieved, reduced, and analyzed following precisely the same procedure outlined in section 3.1 and 3.2 of the main article. The basic properties and the X-ray measurements performed within $1R_e$ apertures of the 49 galaxies from Kim & Fabbiano (2015) are presented in Table A1. For the sake of consistency, we reanalyzed each of the 49 galaxies presented in Kim & Fabbiano (2015), and compared the X-ray measurements within $1R_e$ apertures to those of Su et al. (2015) and the measurements out to large radii with those of Kim & Fabbiano (2015). Overall, our X-ray measurements were in excellent agreement with those of Kim & Fabbiano (2015). For brevity we do not repeat the results here, and defer the reader to Kim & Fabbiano (2015). However, we found several inconsistencies with the gas luminosities and temperatures between the Kim & Fabbiano (2015) and Su et al. (2015) measurements. While not wholly unexpected given the different apertures used in these analyses, at least 11 objects show significant differences in the presented measurements, beyond typical radial variations. Upon further analysis, we deduced that at least eight of the galaxies presented in Su et al. (2015) suffer from significant contamination due to AGN or strong point sources (e.g., LMXBs) close to or at the peak X-ray emission. In many cases these dominate the X-ray emission around 0.5–4.5 keV if the emission is not adequately screened, resulting in erroneously high X-ray temperatures and luminosities. We further deduced that several other low-luminosity objects may have suffered insufficient background subtraction. Given that we find excellent agreement for all of the Kim & Fabbiano (2015) measurements, we elect to use our own $1R_e$ X-ray measurements for those sources where we find significant differences between Kim & Fabbiano (2015) and Su et al. (2015).

Of the 49 galaxies in Kim & Fabbiano (2015) with constrained X-ray measurements, we remove four ATLAS^{3D} objects due to overlap with the MASSIVE sample and five objects due to unconstrained gas measurements within $1R_e$. Specifically, the observation of NGC 3998 suffered from significant X-ray pile-up imparted by a central AGN. NGC 524 was performed on a sub-array that was smaller than $1R_e$. NGC 2778 and NGC 6278 were both undetected in diffuse emission. NGC 1266 appears to have no extended hot gas emission. We note that there are clearly three star-forming knots close to the nucleus of the galaxy, and these dominate the X-ray emission, but we detect no X-ray emission beyond these. Thus, we conservatively choose to remove NGC 1266 from our analyses. Our final comparison ATLAS^{3D} galaxy sample contains 41 sources.

TABLE 3
THE ATLAS^{3D} X-RAY SAMPLE

Common Name	α_{J2000} (deg)	δ_{J2000} (deg)	D_L	R_e	σ_e	L_K	M_{Halo}	λ_{R_e}	ϵ	L_{X,gas,R_e}	T_{X,gas,R_e}	Source
			(Mpc)	($''$)	($km\,s^{-1}$)	(log $L_\odot$)	(log $M_\odot$)			($10^{40}\,erg\,s^{-1}$)	(keV)	
(1)	(2)		(3)	(4)	(5)	(6)	(7)	(8)	(9)	(10)	(11)	(12)
NGC1023	40.1001	39.0633	11.1	47.9	166.7	10.8	13.2	0.391	0.363	0.048 ± 0.004	0.36 ± 0.08	1
NGC2768	137.906	60.0372	21.8	63.1	198.2	11.2	12.9	0.253	0.472	0.73 ± 0.03	0.32 ± 0.06	1
NGC3245	156.827	28.5074	20.3	25.1	209.9	10.8	12.0	0.626	0.442	0.14 ± 0.02	0.31 ± 0.06	1
NGC3377	161.927	13.9856	10.9	35.5	128.2	10.4	13.3	0.522	0.503	0.007 ± 0.004	0.26 ± 0.10	1
NGC3379	161.957	12.5816	10.3	39.8	185.8	10.8	13.3	0.157	0.104	0.008 ± 0.002	0.29 ± 0.10	1
NGC3384	162.070	12.6293	11.3	32.4	130.0	10.6	13.3	0.407	0.065	0.007 ± 0.004	0.25 ± 0.25	2
NGC3414	162.818	27.9750	24.5	24.0	231.7	10.9	12.8	0.073	0.194	0.10 ± 0.02	0.69 ± 0.13	1
NGC3599	168.862	18.1104	19.8	23.4	63.7	10.2	13.4	0.282	0.080	0.019 ± 0.017	0.10 ± 0.10	1
NGC3607	169.228	18.0518	22.2	38.9	206.5	11.1	13.4	0.209	0.185	0.26 ± 0.05	0.41 ± 0.12	1
NGC3608	169.246	18.1485	22.3	29.5	169.0	10.7	13.4	0.043	0.19	0.36 ± 0.06	0.39 ± 0.07	2
NGC3665	171.182	38.7628	33.1	30.9	216.3	11.3	12.0	0.410	0.216	0.92 ± 0.16	0.32 ± 0.09	1
NGC3945	178.307	60.6756	23.2	28.2	182.8	11.0	-	0.524	0.09	0.20 ± 0.04	0.32 ± 0.06	1
NGC4026	179.855	50.9617	13.2	20.4	190.1	10.5	14.2	0.548	0.556	0.015 ± 0.005	0.51 ± 0.36	1
NGC4036	180.362	61.8957	24.6	28.8	188.8	11.1	-	0.685	0.555	0.188 ± 0.037	0.49 ± 0.24	1
NGC4111	181.763	43.0654	14.6	12.0	158.9	10.6	14.2	0.619	0.582	0.330 ± 0.019	0.61 ± 0.06	1
NGC4203	183.771	33.1972	14.7	29.5	129.1	10.6	-	0.305	0.154	0.06 ± 0.01	0.29 ± 0.08	1
NGC4251	184.535	28.1753	19.1	19.5	137.1	10.8	14.2	0.584	0.508	0.030 ± 0.014	0.25 ± 0.15	1
NGC4261	184.847	5.82471	30.8	38.0	265.5	11.3	15.0	0.085	0.222	3.282 ± 0.045	0.79 ± 0.06	1
NGC4278	185.028	29.2806	15.6	31.6	212.8	10.8	14.2	0.178	0.103	0.154 ± 0.006	0.32 ± 0.13	1
NGC4342	185.913	7.05394	23.0	6.6	242.1	10.4	15.0	0.528	0.442	0.041 ± 0.006	0.57 ± 0.12	1
NGC4365	186.118	7.31752	23.3	52.5	221.3	11.2	15.0	0.088	0.254	0.42 ± 0.04	0.49 ± 0.09	1
NGC4374	186.266	12.8870	18.5	52.5	258.2	11.3	15.0	0.024	0.147	3.866 ± 0.053	0.75 ± 0.06	1
NGC4382	186.350	18.1911	17.9	66.1	179.1	11.3	15.0	0.163	0.202	0.629 ± 0.023	0.4 ± 0.07	1
NGC4406	186.549	12.9460	16.8	93.3	190.5	11.4	15.0	0.052	0.211	9.98 ± 1.28	0.81 ± 0.06	2
NGC4459	187.250	13.9786	16.1	36.3	158.1	10.8	15.0	0.438	0.148	0.166 ± 0.013	0.38 ± 0.08	2
NGC4473	187.454	13.4293	15.3	26.9	186.6	10.7	15.0	0.229	0.421	0.049 ± 0.007	0.34 ± 0.1	1
NGC4477	187.509	13.6364	16.5	38.9	148.9	10.8	15.0	0.446	0.135	0.615 ± 0.021	0.33 ± 0.08	1
NGC4494	187.850	25.7750	16.6	49.0	150.0	11.2	14.2	0.212	0.173	0.014 ± 0.13	0.25 ± 0.48	1
NGC4526	188.513	7.69914	16.4	44.7	208.9	11.1	15.0	0.453	0.361	0.50 ± 0.11	0.29 ± 0.02	2
NGC4552	188.916	12.5560	15.8	33.9	224.4	10.9	15.0	0.049	0.047	2.21 ± 0.81	0.6 ± 0.01	2
NGC4596	189.983	10.1760	16.5	38.9	125.6	10.8	-	0.639	0.254	0.15 ± 0.014	0.25 ± 0.12	1
NGC4636	190.708	2.68778	14.3	89.1	181.6	11.0	13.7	0.036	0.094	11.34 ± 0.052	0.73 ± 0.06	1
NGC4697	192.150	-5.80085	11.4	61.7	169.4	10.9	13.6	0.322	0.447	0.232 ± 0.036	0.32 ± 0.04	2
NGC4710	192.412	15.1655	16.5	30.2	104.7	10.6	13.5	0.652	0.699	0.030 ± 0.009	0.14 ± 0.13	1
NGC5198	202.548	46.6708	39.6	24.0	201.4	11.0	10.6	0.061	0.146	0.182 ± 0.173	0.45 ± 0.3	1
NGC5422	210.175	55.1645	30.8	21.4	157.4	10.7	13.6	0.600	0.604	0.017 ± 0.017	0.15 ± 0.8	2
NGC5576	215.265	3.27105	24.8	21.9	155.2	10.9	12.3	0.102	0.306	0.036 ± 0.042	0.49 ± 0.4	2
NGC5813	225.297	1.70197	31.3	57.5	210.9	11.4	13.7	0.071	0.170	32.07 ± 0.37	0.71 ± 0.06	1
NGC5838	226.359	2.09936	21.8	25.1	276.1	11.0	13.7	0.521	0.361	0.332 ± 0.037	0.4 ± 0.1	1
NGC5846	226.622	1.60564	24.2	58.9	223.4	11.4	13.7	0.032	0.062	13.79 ± 0.31	0.72 ± 0.06	1
NGC5866	226.623	55.7633	14.9	36.3	157.0	10.9	12.4	0.319	0.566	0.1210 ± 0.008	0.35 ± 0.09	1

Notes:- [1]Common galaxy name; [2]Galaxy co-ordinates; [3]Luminosity distance in megaparsecs; [4]Optical effective radius in arcseconds(Cappellari et al. 2013); [5]Velocity dispersion measured at R_e in $km\,s^{-1}$ (Cappellari et al. 2011); [6]Logarithm of K-band luminosity in units of solar luminosities (Cappellari et al. 2011); [7]Logarithm of halo mass in units of solar masses (Crook et al. 2007); [8]2-D galaxy rotation parameter; [9]Ellipticity, such that $\epsilon = 1 - b/a$; [10]Gas X-ray luminosity measured with apertures of R_e in units of $10^{40}\,erg\,s^{-1}$; [11]Gas X-ray temperature in units of keV; [12]Source for X-ray measurements: (1) this work; (2) Su et al. (2015).